LRS2: design, assembly, testing, and commissioning of the second-generation low-resolution spectrograph for the Hobby-Eberly Telescope

Chonis, Taylor, Hill, Gary, Lee, Hanshin, Tuttle, Sarah, Vattiat, Brian, et al.

Taylor S. Chonis, Gary J. Hill, Hanshin Lee, Sarah E. Tuttle, Brian L. Vattiat, Niv Drory, Briana L. Indahl, Trent W. Peterson, Jason Ramsey, "LRS2: design, assembly, testing, and commissioning of the second-generation low-resolution spectrograph for the Hobby-Eberly Telescope," Proc. SPIE 9908, Ground-based and Airborne Instrumentation for Astronomy VI, 99084C (9 August 2016); doi: 10.1117/12.2232209

SPIE.

Event: SPIE Astronomical Telescopes + Instrumentation, 2016, Edinburgh, United Kingdom

LRS2 - design, assembly, testing, and commissioning of the second generation low resolution spectrograph for the Hobby-Eberly Telescope*

Taylor S. Chonis[a], Gary J. Hill[a,b], Hanshin Lee[a], Sarah E. Tuttle[a], Brian L. Vattiat[a], Niv Drory[a], Briana L. Indahl[b], Trent W. Peterson[a], Jason Ramsey[a]

[a]The University of Texas at Austin, McDonald Observatory, 2515 Speedway, Stop C1402, Austin, TX, USA 78712;
[b]The University of Texas at Austin, Department of Astronomy, 2515 Speedway, Stop C1400, Austin, TX, USA 78712;

ABSTRACT

The second generation Low Resolution Spectrograph (LRS2) is a new facility instrument for the Hobby-Eberly Telescope (HET) at McDonald Observatory. Designed as a powerful spectroscopic follow-up platform, LRS2 is based on the design of the HETs new Visible Integral-field Replicable Unit Spectrograph (VIRUS) and provides integral field spectroscopy for two seeing-limited fields of $6''\times12''$ with unity fill factor. The replicable design of VIRUS has been leveraged for LRS2 to gain broad wavelength coverage from 370 nm to 1.0 μm, spread between two fiber-fed dual-channel spectrographs that operate in unison but observe independent fields that are separated by $100''$. The blue spectrograph pair, LRS2-B, covers $364 \leq \lambda$ (nm) ≤ 467 and $454 \leq \lambda$ (nm) ≤ 700 at fixed resolving powers of $R = \lambda/\delta\lambda \approx 2500$ and 1400, respectively, while the red spectrograph pair, LRS2-R, covers $643 \leq \lambda$ (nm) ≤ 845 and $823 \leq \lambda$ (nm) ≤ 1056 with both of its channels having $R \approx 2500$. In this paper, a detailed description of the instrument's design, assembly, and laboratory testing is provided in which the focus is placed on the departures from the basic framework of the design and processes previously established for VIRUS. Both LRS2 spectrograph pairs have been successfully deployed on the HET, and commissioning efforts are ongoing. Using on-sky data, the performance of the spectrograph is compared to models of the instrumental sensitivity. The measured performance of LRS2 indicates that the instrument will provide efficient spectroscopic follow-up observations of individual targets, and will be especially powerful when combined with the extensive survey capabilities of VIRUS for HETDEX.

Keywords: Spectrographs: low resolution, Spectrographs: integral field, Hobby-Eberly Telescope, LRS2, VIRUS, HETDEX

1. INTRODUCTION

McDonald Observatory's Hobby Eberly Telescope (HET[1]) is currently undergoing a massive facility upgrade and transformation into a wide-field spectroscopic survey facility in preparation for the ambitious HET Dark Energy Experiment (HETDEX[2]). Over $\sim$ 120 nights starting later this year, HETDEX will blindly amass a spectroscopic sample of $\sim$0.8 million Lyman-α (Lyα) emitting galaxies (LAEs) over a 420 degree^2 field (9 Gpc^3 comoving) to be used as tracers of large-scale structure for constraining dark energy and measuring its possible evolution from redshifts $1.9 < z < 3.5$. To accomplish this, the HET will be outfitted with a revolutionary new survey instrument called the Visible Integral Field Replicable Unit Spectrograph (VIRUS[3]), which consists of 156 copies of a simple fiber-fed integral field spectrograph and leverages the economies of scale associated with large-scale replication to significantly reduce overall costs compared to a similarly capable monolithic instrument. To accommodate VIRUS, the HET has been outfitted with a new, sophisticated wide-field spherical aberration corrector (WFC[4]) as a part of the HET Wide Field Upgrade (WFU[5]), which increases the telescope's field of view

*The Hobby-Eberly Telescope is operated by McDonald Observatory on behalf of the University of Texas at Austin, the Pennsylvania State University, Ludwig-Maximillians-Universität München, and Georg-August-Universität Göttingen.

Further author information: (Send correspondence to G.J.H.)
G.J.H.: E-mail: hill@astro.as.utexas.edu, Telephone: 1-512-471-1477

Ground-based and Airborne Instrumentation for Astronomy VI, edited by Christopher J. Evans, Luc Simard, Hideki Takami
Proc. of SPIE Vol. 9908, 99084C · © 2016 SPIE · CCC code: 0277-786X/16/$18 · doi: 10.1117/12.2232209

to 22′ and increases the telescope's pupil to a full 10 m diameter. The WFC is supported by a new high-precision tracker,[6] and a new Prime Focus Instrument Package (PFIP[7]) that includes a large number of calibration and metrology instruments to keep the telescope operating at optimal focus under closed-loop control.

In the HETDEX era, efficient broadband low resolution spectroscopy will be an especially critical capability at the HET for HETDEX survey follow-up and to support a wide range of other anticipated and legacy research programs. For the past decade, the HET has provided this capability to its users through the Marcario Low Resolution Spectrograph (LRS[8]), which has been a workhorse facility instrument in the optical and near-infrared (NIR) that has provided the majority of the telescope's citations over that time period. As an imaging spectrograph, LRS previously rode on the HET's tracker and was fed directly by the telescope's spherical aberration corrector. However, due to the physical and optical constraints imposed by the new WFC and upgraded PFIP, LRS is incompatible with the upgraded HET and must be replaced by a new fiber-coupled instrument.

The VIRUS unit spectrograph design was intended to be adaptable to a range of spectral resolutions and wavelength coverage configurations. By taking advantage of the large engineering investment already made in VIRUS, a new second generation facility low resolution spectrograph (LRS2) with improved sensitivity, broader spectral coverage, and integral field capability can be realized to replace LRS at a comparable cost to modifying the original instrument for compatibility with the WFU. As a simple and robust general purpose instrument with rapid setup time and high efficiency, a VIRUS-based LRS2 has been designed to be highly complementary to VIRUS and to exploit the queue-scheduled[9] HET for efficient survey follow-up, synoptic observations, and observations of targets of opportunity.

In the following section, the anticipated scientific utility of LRS2 is outlined. In Sec. 3, a technical summary of the instrument design is provided, which focuses on the departures from the base design of the VIRUS unit spectrograph. The assembly, optical alignment, laboratory testing, and characterization of the instrument are described in Sec. 4. LRS2's deployment at the HET and the on-sky performance of the instrument is discussed in Sec. 5. Finally, a summary of LRS2's current status and an outlook towards full scientific operation of the instrument is given in Sec. 6.

2. SCIENCE DRIVERS

LRS2 will enable the continuation of current LRS science programs as well as provide new and improved capabilities associated with a contiguous integral field unit (IFU) input, improved sensitivity, and broader spectral

Observation Type	Science Application	LRS Legacy Reference / Notes
Targets of Opportunity	γ-ray bursts	Schaefer et al. 2003; Racusin et al. 2008
	Supernovae	Zheng et al. 2008
Synoptic Observations	AGN Reverberation Mapping	Kaspi et al. 2007
	Supernovae Fading	Quimby et al. 2007
Survey Follow-Up / Single Object Studies	Supernovae	Dark Energy Survey follow-up; determine redshifts and classification
	Brown Dwarfs	Luhman et al. 2009
	Quasars	Schneider et al. 2000
	Galaxy Structure, Dynamics	Corsini et al. 2008
	Cluster-Cosmology Science	Galaxy cluster surveys to validate cluster-finding algorithms; assess catalog completeness.
	High-z Galaxies to $z < 7.6$	Redshift confirmation, study of young galaxies, probing reionization
HETDEX Follow-Up (AGN, stars, galaxies, clusters, and more to the limit of the SDSS imaging survey)	[O II] Emitters	~1 million [O II] emitters at $z < 0.5$
	Metal Poor Stars	Detailed studies of primitive stellar populations
	Emission Line Object Classification	Broad spectral coverage allows classification via multiple emission lines
	Galactic Winds	Emission line diagnostics and outflow signatures for galaxies at $z < 0.5$
	Lyα Emission Line Science	Radiative transfer studies, Lya blobs, star-forming galaxy physics

Table 1. LRS2's anticipated areas of scientific utility. The science applications with citations are legacy LRS programs.

coverage from near the atmospheric ultraviolet (UV) cutoff to the NIR. While a VIRUS-based LRS2 design will not replicate the imaging or multi-object capabilities of LRS, the majority of LRS usage has historically been spectroscopic slit observations of individual small objects (i.e., $< 10''$ in size). Additionally, the imaging capability previously provided by LRS will be assumed by the new acquisition camera that is included as part of the new PFIP[7] while wide field, multi-object spectroscopy will be carried out with VIRUS.[3] The driving requirements for LRS2 are broadband spectral coverage with improved throughput (particularly in the red) and excellent sky subtraction. LRS has historically been the dominant instrument in dark time and has been used for the largest variety of science applications among the three current HET instruments (see Ref. 10). LRS2 is expected to have similar broad application and to increase the efficiency of many of the tasks at which its predecessor excelled. Additionally, the change from a slit to an IFU and the enhanced red sensitivity will enable a range of new science applications.

When coupled with the responsive queue scheduling[9] of the HET, LRS has proven to be an ideal instrument for time critical studies of transient phenomena, synoptic observations, and follow-up studies of objects discovered in large surveys. LRS2 will increase these capabilities with its wider spectral coverage and IFU input, the latter of which will significantly decrease acquisition and setup times. Additionally, a contiguous-field IFU adapts the data to any image quality without losing light at the entrance aperture.

LRS2 will play a uniquely important role as a follow-up instrument for interesting objects found through upcoming large surveys that will discover an unprecedented number of objects that will require spectroscopic follow-up (e.g., the Dark Energy Survey[†], Pan-STARRS[‡], and the Large Synoptic Survey Telescope[§]). In addition to detecting $\sim$ 1 million LAEs from $1.9 < z < 3.5$, HETDEX[2] will also discover as many [O II] emitters at $z < 0.5$. It will also deliver spectra of large numbers of AGN, stars, galaxy clusters, and more down to the imaging sensitivity limit of the Sloan Digital Sky Survey. The sensitivity limits of LRS2 within a single HET track ($\sim$ 1 hour; see Sec. 5.2) also reach this limit. The unique HETDEX data set will require follow-up with LRS2 to establish, for example, the classification of emission line objects and extremely metal poor stars, and to study emission line diagnostics over a wide wavelength range. For example, Hα, [N II], and [S II] emission line diagnostics will be within the LRS2 bandpass for all HETDEX [O II] emitters. Understanding galactic winds is also an upcoming field, and HETDEX will provide a substantial sample of blue compact dwarf galaxies at $z < 0.5$ where LRS2 can search for the emission line diagnostics of outflows over a wide wavelength range at a moderate resolving power of $R = \lambda/\delta\lambda \gtrsim 2500$.

Table 1 provides a high-level compilation of LRS2's anticipated areas of scientific utility, with citations that refer to legacy LRS programs, where applicable (Refs. 11–17). A more complete summary of these science applications is provided by Ref. 18. Note that the incompleteness of this list is explicitly acknowledged since it is often difficult to predict the wide range of science applications that are accessible to a general purpose facility instrument like LRS2.

3. INSTRUMENT DESIGN

LRS2's design has previously been described in detail in Ref. 18 and Refs. 19, 20, but a summary of the design is provided here for the reader's convenience. LRS2 is based on the VIRUS unit spectrograph design that has been optimized for mass production. As a result, LRS2 will greatly benefit from the investment made in the development and production-line engineering of VIRUS. To begin, the key design features of VIRUS[3] that form the basis of LRS2 are summarized. The departures from the VIRUS baseline that morph it into LRS2 are then discussed in the subsections that follow. VIRUS is summarized schematically in Fig. 1.

3.1 VIRUS: The Building Block of LRS2

The VIRUS unit spectrograph is fiber optically fed and is optimized to accept a $f/3.65$ input beam. The optical design (see Fig. 1*d*) is a double-Schmidt, with the collimator reversed. The Schmidt collimator and camera share a corrector plate and utilize a volume phase holographic (VPH) grating[21] for dispersion at the pupil.

[†]The Dark Energy Survey - *http://www.darkenergysurvey.org/*

[‡]Pan-STARRS - *http://pan-starrs.ifa.hawaii.edu/*

[§]Large Synoptic Survey Telescope - *http://www.lsst.org*

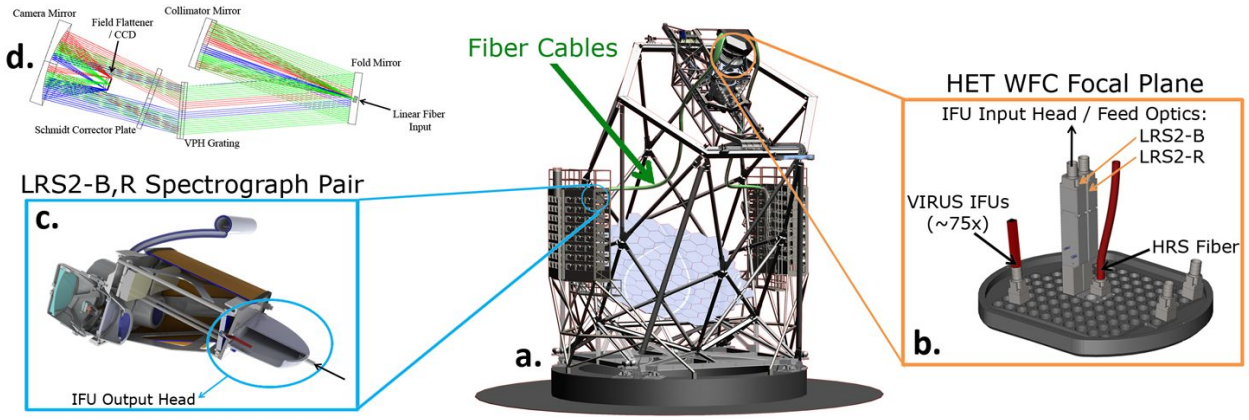

Figure 1. A schematic summary of the VIRUS instrument. *a*) A visualization of the upgraded HET. The large boxes on either side of the telescope structure are environmentally controlled enclosures where the VIRUS spectrographs are stored in operation. *b*) At the focus of the HET WFC above the shutter is the IHMP where the 78 VIRUS IFUs and fiber feeds for other facility instrument (including LRS2) are mounted. *c*) A section view of a VIRUS spectrograph unit pair. *c*) The optical design of a VIRUS spectrograph channel with major components labeled.

The focal reduction factor is 2.8×. For HETDEX, the wavelength coverage is $350 < \lambda\,(\mathrm{nm}) < 550$, but the design is largely pan-chromatic since the optical power is mainly in the two spherical mirrors. For adaptation to different wavelength ranges, the mirrors and transmissive optics can be supplied with different coatings and custom aspheric correcting optics can be fabricated. The dispersion and wavelength coverage can be further adapted by using grisms instead of a standard VPH grating. The original VIRUS spectrograph design is fed by a "densepak" IFU, where the fibers are arrayed in a hexagonal pattern with a 1/3 spatial fill-factor at the input from the telescope focal plane. For input into the instrument, the fibers are arranged in a linear "slit" pattern. The VIRUS IFU is fed directly at $f/3.65$ by the HET WFC, which projects the 266 μm core diameter fiber into 1.5″ on-sky. An observation with VIRUS consists of three exposures, each in one of three dither positions separated by $\sim 1''$ that fill in the sky coverage gaps between the fibers. In production, each VIRUS mechanical unit contains a pair of spectrographs in a common housing that are fed by a single IFU (see Fig. 1*c*). Since this configuration allows a pair of spectrographs to share common components (such as CCD electronics, vacuum vessels, cryogenic components, etc.), costs are reduced and more efficient use of the limited volume available at the telescope structure is allowed for. Two of these unit pairs will form the basis of the LRS2 instrument. A single prototype VIRUS spectrograph (the Mitchell Spectrograph, formerly VIRUS-P[22]), has been in regular use as a facility instrument on the McDonald Observatory 2.7 m telescope since 2007. In addition to verifying the VIRUS concept, it has resulted in the successful completion of the HETDEX Pilot Survey[23] in preparation for HETDEX. The Mitchell Spectrograph has demonstrated the high throughput, excellent image quality, low ghosting, and exceptional stability of the VIRUS design.

3.2 Channel Wavelength Separation

The original LRS2 design concept[19] utilized two VIRUS unit pairs (i.e., four total spectrograph channels) to simultaneously cover $350 < \lambda\,(\mathrm{nm}) < 1100$ at a fixed resolving power of $R \approx 1800$ through a single $12''\times7''$ contiguous-field IFU. The wavelength separation between the four channels was provided by a single IFU input that included an arrangement of three optimized dichroic beam splitters. However, this design was complicated by the tight space constraints on the HET focal plane and the required alignment tolerance of the input. Additionally, the combination of the required spectral resolution and the constraints imposed by the existing VIRUS optomechanical design would have complicated the data quality near the important Hα emission line. Combined with the large difference in background levels between the UV and NIR, and the typical spectral energy distributions of common astronomical targets, splitting the total wavelength range with significant overlap around Hα was deemed to be an acceptable compromise between science goals and engineering complexity.

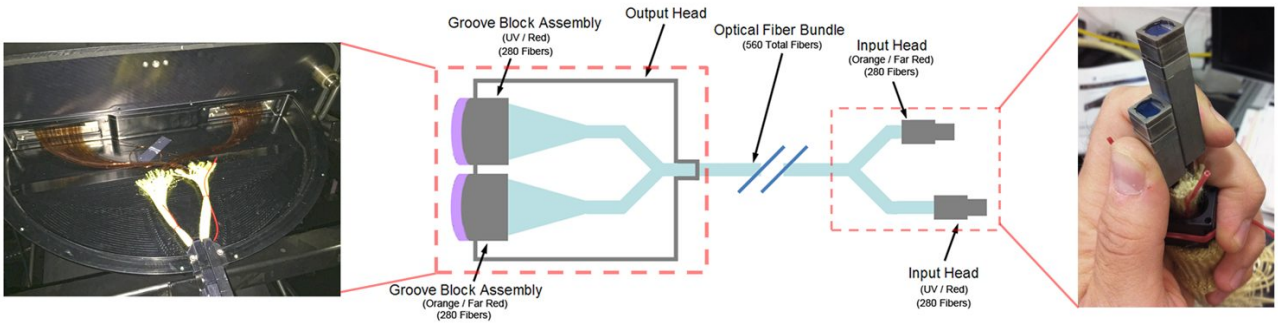

Figure 2. A schematic showing the basic design of the LRS2 IFU fiber cables. The photo at left shows the output head with the cover removed to reveal the fibers fanning out into the virtual slits. The photo at right shows the two input heads that route into the same fiber cable conduit.

As a result, LRS2 now consists of two optimized double-spectrographs, each of which have their own independent inputs at the HET focal plane that each contain a sharp dichroic beam splitter that separates the light into two optimized spectrograph channels (see Refs. 18 and 20). The blue-optimized spectrograph pair (hereafter, LRS2-B; nominally covering $365 - 700$ nm) and the red-optimized pair (hereafter, LRS2-R; nominally covering $640 - 1050$ nm) will overlap significantly in wavelength around the Hα line. Due to the fixed VIRUS spectrograph design into which LRS2 is being adapted, there is a trade-off between spectral coverage and spectral resolution for each of the four spectrograph channels for a given fiber core diameter. Additionally, the cross-over wavelengths of the two dichroic beam splitters must be chosen to minimize the science impact since there is an inevitable loss of data quality around the wavelengths of the split.

Emission line diagnostics in the local universe has historically been a significant use of LRS. To provide continuity to observers in the LRS2 era, the LRS "G2" configuration[8,24] shall be replicated in a single LRS2 channel. This mode provides sufficient wavelength coverage to simultaneously observe Hβ to Hα at $z = 0$ with contingency for a small range in redshift and for accommodating the broad line widths often observed in AGN. This constraint places the channel transition for LRS2-B at ~ 465 nm. With a lower wavelength limit just below [O II] at $z = 0$, LRS2 extends the capability of LRS into the UV by ~ 50 nm, and enables LAE follow-up studies for $2 \lesssim z \lesssim 2.7$ (i.e., the redshift range in which the important rest-frame optical transitions are shifted into the atmospheric windows in the NIR) at a higher spectral resolution for examining Lyα emission line profiles. The bluer LRS2-B channel is thus called the "UV Arm", while the LRS "G2"-replicating channel is referred to as the "Orange Arm".

For LRS2-R, the specific choice of the transition wavelength is less important than maintaining an adequately high spectral resolution in both channels to ensure good sky subtraction since the strong night sky emission bands dominate the background in that wavelength range. As a result, LRS2-R's channel transition shall be located at ~ 850 nm. The bluer LRS2-R channel is referred to as the "Red Arm" and the redder channel as the "Far Red Arm".

Other than a new, highly customized IFU described below, LRS2-B requires only modest adaptation of the VIRUS design. LRS2-R requires similar modifications to LRS2-B in addition to different optical coatings, optimized refractive camera correcting optics, and custom red-sensitive charge-coupled device (CCD) detectors.

3.3 Fiber Integral Field Units

The most significant departure from VIRUS for LRS2 is the fiber IFU design and how it is fed by the HET WFC. A contiguous-field IFU is required for LRS2 to ease target acquisition and provide adequate sky sampling for small objects in all image quality conditions, which requires reimaging the telescope's fast $f/3.65$ beam. In addition to the two LRS2 IFU feed assemblies (one for LRS2-B, and one for LRS2-R), the focal plane of the upgraded HET is populated by the fiber feeds for the other HET facility instruments[10,25] and 78 VIRUS IFUs[26] (see Fig. 1*b*). The resulting tight focal plane space constraints require a unique reimaging solution for the LRS2 IFU.

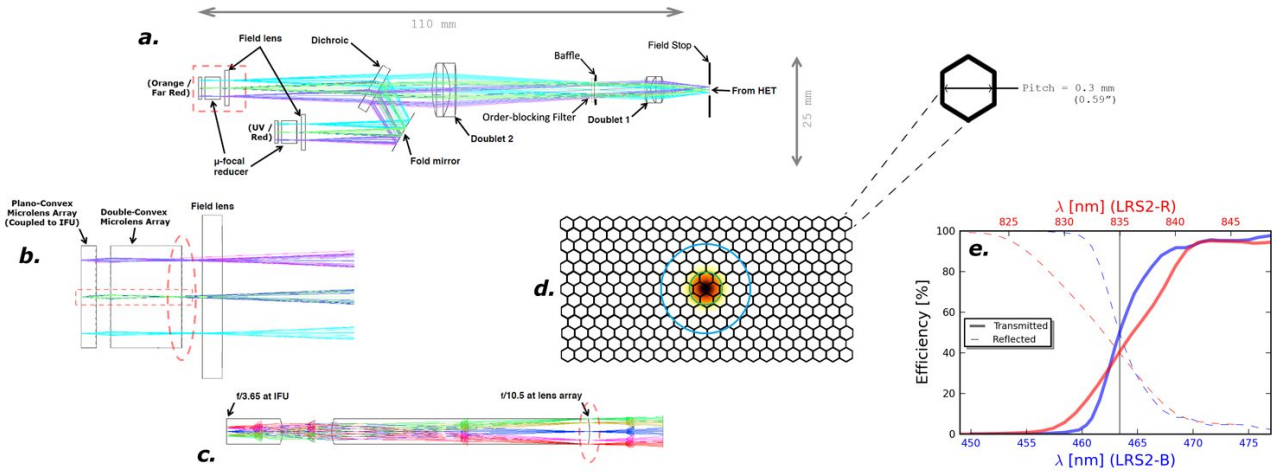

Figure 3. Schematic overview of the LRS2 IFU input optics. *a*) A ray trace of the IFU input optical design with major components labeled. Note the scale. *b*) A detailed view of the microfocal reducer, which consists of a field lens and two lenslet arrays. The optical path of a single spatial element is detailed in Panel *c*, while the spatial layout of the microlens array and definition of the spaxel pitch is shown in Panel *d*. *e*) The transmissivity and reflectivity of the dichroics for LRS2-B (bottom horizontal axis in blue) and LRS2-R (top horizontal axis in red).

3.3.1 Fiber Cables

Each LRS2 spectrograph pair will rely on the well-established VIRUS IFU cable design.[26] This design has been shown to be quite robust, and has successfully passed the equivalent of 10 years of operational moves without displaying any significant decay in its optical properties.[27] For higher spectral resolution, finer spatial sampling, and high broadband transmission, the LRS2 IFUs are constructed with 170 μm core diameter Polymicro FBP fiber. The number of spatial elements in the final IFU design is limited by the number of spectra that can be packed onto the CCDs with sufficient separation for clean extraction. For the VIRUS spectrograph design with 170 μm core diameter fiber, this number is 280 per spectrograph channel. The overall length of the LRS2 fiber cables are 18 m.

At the LRS2 input, the light will be split spectrally using a dichroic before the fibers are initially fed (see below), so each spectrograph channel has its own input fiber head of 280 fibers. The fibers from the two input heads are bundled together through a single conduit and routed to the spectrograph pair together. Using the VIRUS output head design with a custom stainless steel "groove block" that sets the angular fiber spacings, the fibers are separated and arranged into the linear "slits" to feed the respective wavelength-optimized spectrograph channels. The LRS2 fiber cable design is depicted in Fig. 2.

LRS2 Channel	Dichroic Crossover	Feed Optics	Fibers	Active Lenslet Array Format	IFU Size	Order Blocking Filter	Coupling Efficiency	Channel Registration
UV	463.9 nm	Focal Ratio: f/10.5 Micro-image diameter: 120 μm	Core diameter: 170 μm 280 fibers per channel Polymicro FBP 18 m long cable	22 x 13 rectangular array 0.30 mm hexagonal pitch (0.59" on-sky)	6.3 mm x 3.1 mm 12.4" x 6.1" Center to center	None	58.2%	Translation: 0.50±0.03 pitch Rotation: <0.3° Magnification: <0.5%
Orange							79.8%	
Red	835.0 nm					587 nm cut-on 2.8×10^{-3} suppression (at λ <500 nm)	80.7%	Translation: 0.49±0.04 pitch Rotation: <0.3° Magnification:< 0.5%
Far Red							86.9%	

Table 2. LRS2 Feed Optics and IFU Properties.

3.3.2 IFU Feed Optical Design

Fig. 3 shows the optical layout of the IFU input optical system for LRS2. The optical design is the same for LRS2-B and LRS2-R except for the anti-reflective (AR) lens coatings, fold mirror coating, and dichroic design. The IFU input consists of a focal extender made with two custom fused silica / LLF1 doublets mounted after the telescope focus to convert the WFC's $f/3.65$ beam to $f/10.5$ for finer spatial sampling. The two doublets are 6 mm and 12 mm in diameter, respectively. The field of view of the focal extender is $\sim 14''$ in diameter. The image quality of the dual-doublet relay is excellent with 90% of the diffraction encircled energy enclosed within $< 0.25''$ diameter across the central $12''$ of its field of view. The LRS2-R focal extender contains an order blocking filter that is mounted on a knife-edge baffle at the intermediate pupil in between the doublets. The filter is made from AR-coated Schott OG570, which provides a measured transmission of > 0.95 for wavelengths > 680 nm. The 50% cut-on wavelength of the delivered filter is 587 nm, with transmission of 2.8×10^{-3} to provide order blocking for wavelengths < 500 nm. An optimized dichroic after the reimaging doublet splits the beam and reflects bluer light. For LRS2-B and LRS2-R, the as-built dichroic transition wavelength (i.e., the wavelength at which the transmissivity and reflectivity of the dichroic are equal) is 463.9 nm and 835.0 nm, respectively. In Fig. 3*e*, the transmissivity and reflectivity of the dichroics are shown. The transition from reflection to transmission is very sharp and decreases from 80% to 20% reflectance in 4 nm and 7 nm for LRS2-B and LRS2-R, respectively.

After the dichroic split (and subsequent reflection for the bluer channel), each beam is focused onto a microfocal reducer, which reimages the $f/10.5$ beam back to $f/3.65$ to directly image the sliced field onto individual fiber ends by way of an 8 mm diameter fused silica field lens. The microimages are 120 μm in size. As shown by the ray-trace in Fig. 3, the microfocal reducer consists of two fused-silica microlens arrays which provide the field slicing with a 95% fill-factor. The convex microlens surfaces are all spherical, and the elements are hexagonal with a pitch of 0.3 mm ($0.59''$ on-sky). The IFU layout consists of 13 rows of fibers which alternate between 22 or 21 individual fibers (see Fig. 3*d*). This covers a $12.4'' \times 6.1''$ field (physically, 6.3 mm $\times$ 3.1 mm) as measured from the centers of the microlens elements. The elongated field is advantageous as it places sky fibers farther from the observed object (depending on its size, shape, and placement on the IFU).

High quality modern optical fibers exhibit little enough focal ratio degradation (FRD) when fed at $f/3.65$ that the telescope's central obstruction should be maintained in the spectrograph for directly illuminated fibers,[28] as long as the fibers have not been stressed or damaged. Since central obscurations exist in the LRS2 spectrograph due to its folded collimator and Schmidt camera, the retention of the telescope's central obstruction within the spectrograph should result in better throughput. As a result, direct imaging onto the fiber ends with the microfocal reducer design described here results in higher performance compared to the more traditional method of lenslet coupling, which forms micropupil images onto the fibers (e.g., Ref. 29). Another advantage of the microfocal reducer design is that it is telecentric, which results in less sensitivity to alignment errors that could result in additional losses and effective system FRD. Modeling of the microfocal reducer-based IFU feed design predicted an overall fiber coupling efficiency of $\sim 90\%$, including diffraction effects. The fiber feed optics and IFU properties are summarized in Table 2.

3.3.3 IFU Feed Mechanical Design

The mechanical design of the IFU input head and feed assembly is shown in Fig. 4. It consists of four stainless steel subassemblies: the first houses the dual doublet focal extender, the second houses the dichroic and fold mirror, and positions the two IFU input heads. The remaining two subassemblies are the two IFU input heads, which include the mechanical framework for positioning the optics of the microfocal reducer.

For the focal extender and dichroic subassemblies, the optics can be positioned and secured to sufficient accuracy by using mechanical positioning features fabricated with precision machine tolerances through use of wire electrical discharge machining (EDM). Positioning the optics of the microfocal reducer with sufficient accuracy with respect to the fiber array is much more challenging. The 280 fibers are coupled to the alloy hole block in the same way as the VIRUS IFUs.[26] The two microlens arrays and the field lens are aligned to the fiber array using a custom 8-degree of freedom alignment jig that is equipped with a machine vision camera to monitor the alignment of reference features that are drilled into the hole block and precision etched into each of the microlens arrays by the vendor. The wire EDM-machined frames for the microlens array and field lens are epoxied into place once alignment has been achieved.

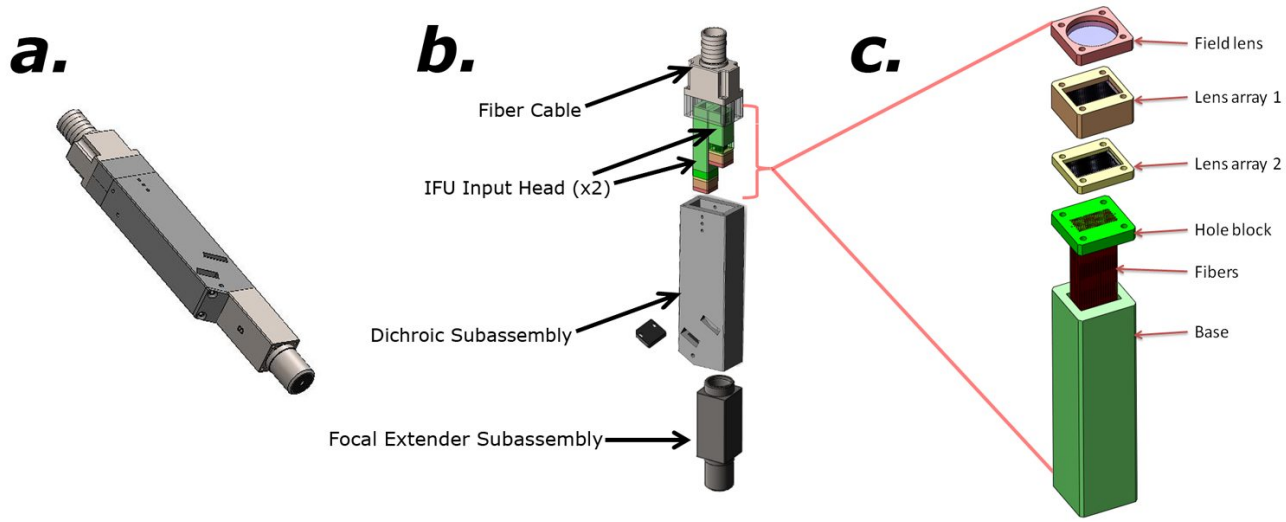

Figure 4. The IFU input mechanical assembly is shown in Panel a, and an exploded view with major subassemblies labeled is shown in Panel b. Panel c shows an exploded view of one of the two input head assemblies.

Once the microfocal reducer optics have been aligned and assembled onto the fiber array, the two assembled input heads are inserted into the sleeve that houses the dichroic and fold mirror. The registration of the two IFUs must be accurate to within a fraction of the lenslet pitch for spatially resolved studies of extended objects to ensure that each spectrograph channel is measuring the same field of view. Precision machining of the two perpendicular inner walls of the sleeve and the outside walls of the two input head bases ensures that this registration requirement is satisfied.

3.4 VPH Grisms

The mechanical framework of a VIRUS unit spectrograph provides little freedom to change the collimator and camera angles. As a result, VPH grisms[24] are utilized to redirect the diffracted beam into the camera aperture since each LRS2 channel utilizes a disperser with a fringe frequency that differs from VIRUS to achieve the individual wavelength coverage configurations. For a review of VPH grating physics, see Ref. 30 and the references therein. The optical path through an LRS2 grism is shown in Fig. 5a. Symbols described in the following subsection also refer to this figure.

3.4.1 Grism Optical Design

For all four LRS2 grisms, the prisms and VPH grating substrates are fabricated from BK7 glass with AR coated external optical faces. The grisms are used in first order, and the grating layer clear aperture is circular with an over-sized 138 mm diameter to relax the translational position tolerance within the instrument. The grisms have a square physical footprint with 150 mm sides.

The grism optical design starts with the desired wavelength coverage for each channel. From this, the required dispersion is calculated and a good estimate of the required fringe density G_Λ can be determined. Using the Bragg condition, the optimal angle of incidence on the grating layer α_{DCG} is calculated for maximizing the diffraction efficiency at the wavelength of choice. Given α_{DCG}, the angle of diffraction $\beta_{\rm DCG}$ is calculated for the central wavelength, which dictates the total wedge angle γ of the grism assembly to match the diffracted beam deviation to the fixed angle of 24.3° between the collimated beam and the camera optical axis ($\theta_{\rm VIRUS}$). For each channel except the LRS2-B Orange Arm, γ is relatively large and requires a prism to be bonded to both sides of the VPH grating (each individual prism has the same wedge angle, i.e., $\gamma_a = \gamma_b = \gamma/2$). Since the beam deviation for the Orange Arm grating only requires $\gamma = 3.5°$, a single prism is bonded to the backside of the grating. The largest required γ is for the Far Red Arm at 37.4°.

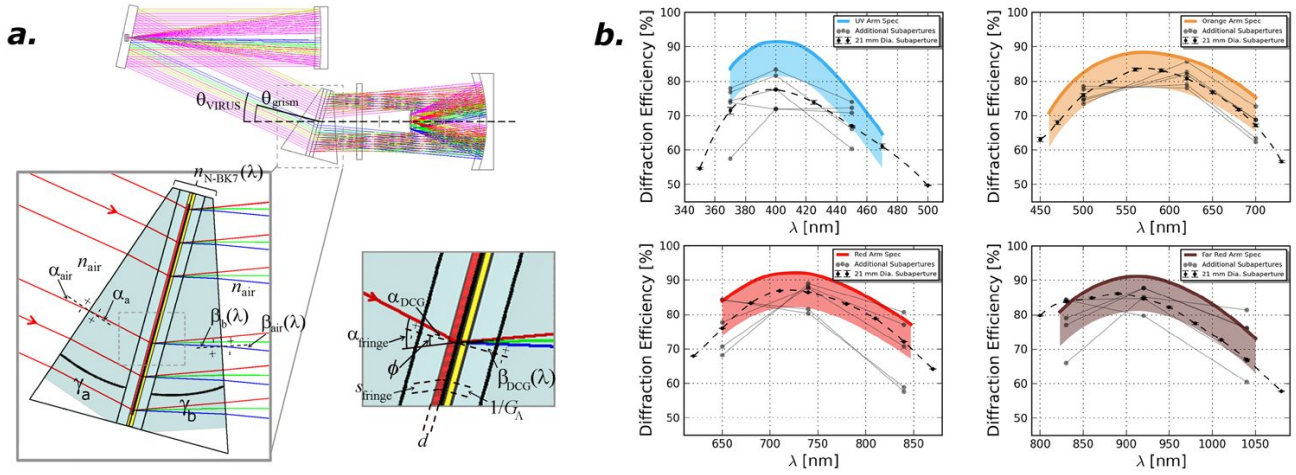

Figure 5. *a*) A ray trace through an LRS2 VPH grism assembly. Various angles are marked in this schematic to clarify the description of the optical design that is presented in Sec. 3.4.1. *b*) RCWA predictions of the first order external diffraction efficiency of each grism assembly for unpolarized light. The colored curve represents the diffraction efficiency of the nominal design, while the shaded region shows the acceptable margin. The dashed curve shows the mean diffraction efficiency, as measured in tests described in Sec. 4.1. Gray data points represent measurements of individual subapertures to illustrate the delivered level of uniformity.

The physical tilt of the grism assembly $\theta_{\rm grism}$ is constrained by the need to avoid imaging the Littrow recombination ghost.[31] This requires decoupling the Bragg condition from the Littrow configuration, and is achieved by introducing a tilt ϕ to the fringes. The amount of fringe tilt is a free parameter, and is selected to yield the proper value of $\alpha_{\rm DCG}$ for meeting the Bragg condition given the constraints of γ and the $\theta_{\rm grism}$.

The dichromated gelatin (DCG) diffracting layer has been carefully designed such that the external diffraction efficiency is relatively uniform across the channel bandpass, and that the peak efficiency is $\gtrsim 80\%$ through the entire grism assembly near the central wavelength. In Fig. 5*b*, predictions of the first order external diffraction efficiency of each grism assembly as calculated using Rigorous Coupled Wave Analysis (RCWA[32]) are shown for unpolarized light. The nominal design properties of the grisms including the DCG layer parameters are summarized in Table 3. A rigorous Monte Carlo optical tolerance analysis of the assemblies indicates that the grisms are straightforward to fabricate.

Property	UV	Orange	Red	Far Red
$\theta_{\rm VIRUS}$	24.3° (nominal) – 0.6° (shim)		24.3° (nominal) – 0.4° (shim)	
$\theta_{\rm grism}$	15. 3°	14.3°	15.3°	15.3°
$\gamma_{\rm tot}$	35.5°	3.5° (γ_a = 0°)	30.8°	37.4°
Grism Dimensions	150 mm x 150 mm footprint, 138 mm clear aperture diameter			
Measured Fringe Frequency G_Λ	1764 lines mm^{-1}	770 lines mm^{-1}	918 lines mm^{-1}	792 lines mm^{-1}
Fringe Tilt ϕ	-1.31°	-2.00°	-2.06°	-2.09°
DCG Layer Thickness d	3.5 µm	6.0 µm	4.9 µm	7.5 µm
Incident Angle on DCG $\alpha_{\rm DCG}$	12.04°	6.57°	11.17°	12.28°
DCG Index Modulation $\Delta n_{\rm DCG}$	0.060	0.048	0.074	0.061
Diffraction Efficiency	72.0% at 370 nm 77.3% at 400 nm 68.4% at 450 nm	75.8% at 500 nm 81.3% at 620 nm 67.2% at 700 nm	76.8% at 650 nm 85.5% at 740 nm 69.5% at 840 nm	78.9% at 830 nm 85.0% at 920 nm 71.3% at 1040 nm

Table 3. Designed properties of the LRS2 VPH grisms. The diffraction efficiency values are measured (see Sec. 4.1).

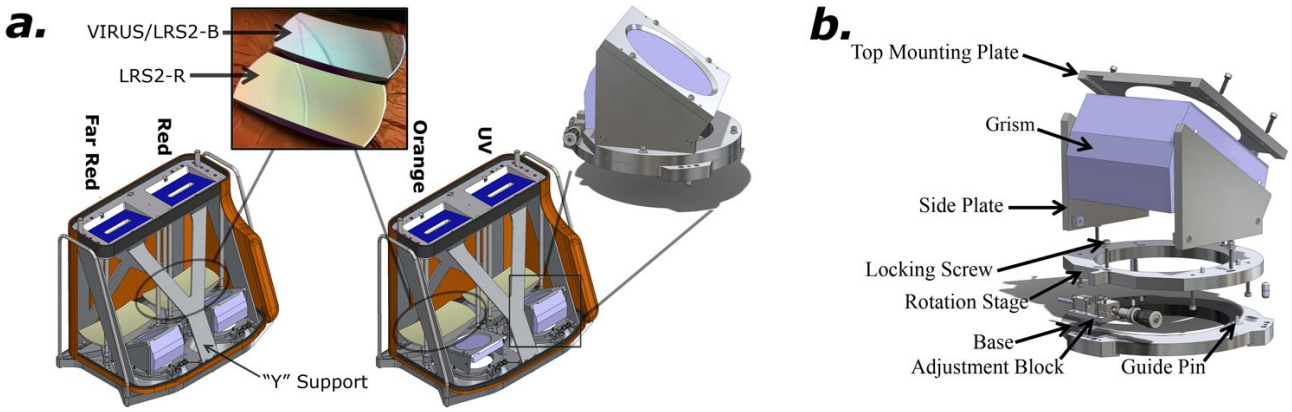

Figure 6. *a*) An overview of the LRS2 collimator assemblies. A photo of the collimator mirror for LRS2-B and LRS2-R is also shown to illustrate the visual difference between the two dielectric coating specifications. The grism mount design is also highlighted. *b*) An exploded view of the grism mount with major components labeled.

3.4.2 Grism Mount Design

The Monte Carlo optical tolerance analysis that was mentioned above also considered the alignment tolerance of the positioning of the grism within the instrument. The installation tolerance is sufficiently loose that adequate alignment can be achieved by primarily using precision machined reference features. Only a single fine adjustment of the rotation of the grism assembly about the camera's optical axis (within $\pm 0.75°$) is necessary to compensate for angular misalignments within the grism assembly during fabrication. A model of the resulting 6061 aluminum mounting cell design can be seen in Fig. 6. The design consists of two primary subassemblies: the mount base assembly (which provides the required fine angular adjustment capability), and the top assembly. While the former was designed to be universal for all four grism mounts, the latter is specific to the unique geometry of each individual grism. The top mask plate contains the mechanical reference features for properly orienting the grism, and for setting the thickness of the RTV adhesive layer (0.5 mm) that bonds the front prism face outside of the CA to the underside of the plate. An elliptical knife-edge baffle is also included to reduce stray light.

Utilizing design heritage[33] from VIRUS, the rotation stage of the mount base assembly consists of two press-fit guide pins in the mount base plate that slide within arced slots on the rotation stage plate. The fine adjustment is achieved by a micrometer and opposing spring plunger that push on a tab extrusion on the rotation stage plate. The rotation stage plate rides on a series of 6 nylon pads to provide smooth motion. Once aligned, the rotation stage plate is locked with a series of 4 locking screws, which consist of nylon and stainless steel washers along with a split lock washer. The base plate features the same footprint and locating pin scheme as a VIRUS grating cell to allow the LRS2 grism cell assemblies to fit onto the production VIRUS collimator base plates with minimal modification.

3.5 Collimator Assembly

Other than the change from standard VPH gratings to the larger grisms, the two LRS2 collimator assemblies remain optically and mechanically unchanged from the standard VIRUS design. Due to interference with the larger grism optics, the only mechanical exception is the exchange for a "Y"-shaped support strut on the lower side of the standard VIRUS collimator assembly, which is a more accommodating design. All of the reflective optics in the LRS2-B collimator assembly utilize the same broadband dielectric coating used in VIRUS ($> 95\%$ average reflectivity for $345 - 700$ nm; optimized for $350 - 590$ nm at $> 98\%$ average reflectivity). In LRS2-R however, the reflective optics are custom coated with a red-optimized dielectric coating ($> 98\%$ average reflectivity for $650 - 1050$ nm). The collimator assembly can be seen schematically with the grism mounting cells in Fig. 6.

3.6 Cameras & Detectors

Like the LRS2 collimator assemblies, only minor modification is needed to convert a VIRUS camera pair into an LRS2 camera pair. A more detailed description of the VIRUS camera and detector system design is provided by

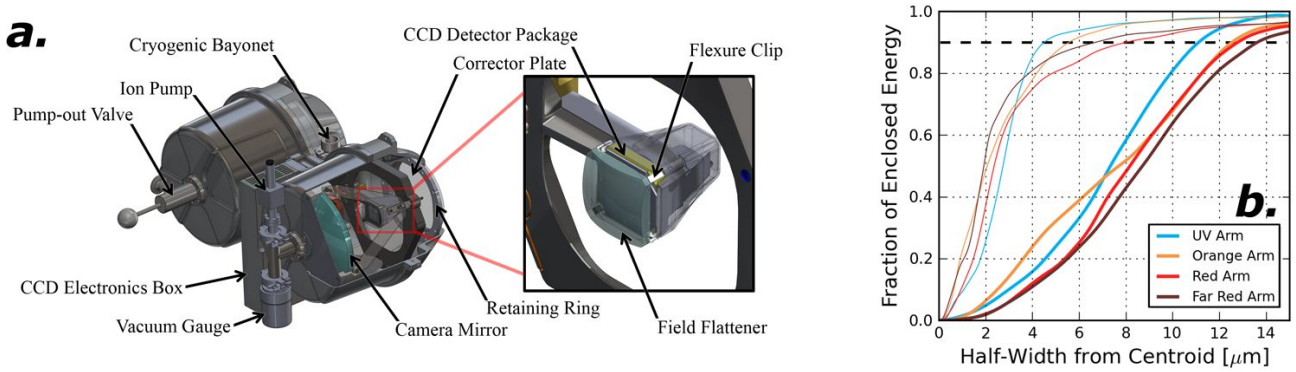

Figure 7. *a*) LRS2 camera pair solid model, which shows a section view into one of the cameras to reveal the detector, optics, and other internal components. The detector package is highlighted in the inset, and major components are labeled. *b*) The best (thin curves) and worst (thick curves) modeled diffraction ensquared energy of the camera system at the CCD detector for each LRS2 channel.

Ref. 3. An overview of an LRS2 camera pair can be seen in Fig. 7*a*.

3.6.1 Optomechanical Modifications

The camera's Schmidt optical design relies on transmissive, aspheric fused silica optics to correct for various aberrations that are inherent in the spherical camera mirror and to flatten the focal plane. At wavelengths $\gtrsim 550$ nm, the image quality of the base VIRUS camera design begins to degrade due to the change in the index of refraction of the fused silica. For LRS2, the image quality requirement is $\geq 90\%$ diffraction enclosed energy (EE90) from a point source within a 2×2 pixel area (i.e., 30 μm $\times$ 30 μm) for all imaged wavelengths and field angles. Meeting this requirement is important to avoid fiber cross-talk, especially at longer wavelengths where bright night sky emission lines become a factor.

For LRS2-B, no departure from the VIRUS camera optical design is required since its wavelength coverage lies mostly within that of the base VIRUS design. For LRS2-R, modifications of the field flattener and corrector plate design is required. However, the change in the index of refraction of fused silica over the wavelength coverage of both LRS2-R channels is small enough that a single optical prescription for its camera transmissive optics can be found. The optimal LRS2-R corrector plate has a different front aspheric surface and a smaller central thickness. The optimal LRS2-R field flattener has a much stronger asphere on the back side of the optic, a smaller central thickness, and a larger radius of curvature on the front spherical optical face. Since these LRS2-R prescriptions change the edge thicknesses compared to the standard for VIRUS, the mounting hardware (Invar flexure clips for the field flattener, and aluminum retaining ring for the corrector plate) also required minor mechanical modifications. The final modeled image quality is shown along with LRS2-B's in Fig. 7*b*.

As with the LRS2-R collimator mirrors, the camera mirrors for the two LRS2-R channels are coated with the same high reflectivity dielectric coating that is optimized for $650 - 1050$ nm. Similarly, the LRS2-R transmissive camera optics also have custom AR coatings that are optimized for this wavelength range.

3.6.2 Detector System

The LRS2-B cameras utilize the same cryogen cooled, thinned, and backside illuminated 2064×2064 CCD detectors with 15 μm square pixels as VIRUS. For LRS2-R, custom CCDs with identical physical format and read-out electronics are utilized. These CCDs have bandpass-optimized AR coatings and a thicker epitaxial layer to help mitigate charge diffusion effects, boost sensitivity at longer wavelengths, and reduce fringing. All four LRS2 CCD detectors feature low read-noise, low dark current, and high quantum efficiency (QE).

The CCD controllers and other detector system electrical components are identical to those for VIRUS that are supplied by Astronomical Research Cameras, Inc. However, the LRS2 detector system operates independently and is significantly scaled-down in terms of the level of multiplex. Like VIRUS, however, the first layer of

multiplexing takes place on the CCD detector, where each half of the detector is read-out through a separate amplifier. The read-out of the pair of CCDs within the shared cryostat is controlled by the same CCD controller, which connects directly through the cryostat housing without cables by way of a 55-pin hermetic bulkhead connector. Each controller has DC power in and fiber-optic data lines out.

DC power is supplied through an existing VIRUS power supply in the enclosure that houses the two LRS2 spectrograph pairs using two power leads from one of the three junctions on the power supply filter box. For LRS2, a single dedicated multiplexer unit (MUX) for the four detectors will be used, which synchronizes the timing of the CCD clocks and feeds the data from all four CCD detectors to a single PCI card, which is integrated directly into the LRS2 Control Computer. This is a dedicated machine for controlling LRS2 and its associated equipment, as well as transmitting and receiving LRS2 related functions and data to and from the HET telescope control system (TCS[34]). The detector control system can read all four LRS2 CCDs in ~ 40 seconds in 1×1 binning mode.

The LRS2 cameras are outfitted with full range vacuum gauges and ion pumps which operate as a self-enclosed subsystem of the instrument and are remotely controlled through the LRS2 Control Computer. The typical operational pressures of the LRS2 cameras while cold are $\sim 10^{-6}$ to 10^{-7} Torr. The attachment of the gauge and ion pump to the cryostat can be seen in Fig. 7*a*. Experience with LRS using a similar subsystem showed that ion pumping during daylight hours allowed a cold camera to maintain acceptable operating pressures for up to $\sim$18 months.

3.7 Operational Concept

The two LRS2 IFU feeds are integrated just off-center of the upgraded HET's $22'$ field of view on the same focal plane assembly on which all of the VIRUS IFUs are mounted, otherwise known as the Input Head Mount Plate (IHMP; see Fig. 8*a*). The center-to-center angular distance from the LRS2-B IFU field to LRS2-R's is $100''$. LRS2 and VIRUS thus share the same external shutter system that is controlled through the TCS. This allows the implementation of parallel observing[35] where VIRUS can observe in the background while one of the LRS2 spectrograph pairs are observing their target. In most cases, the LRS2 observations will drive the parameters of the simultaneous observation, and VIRUS will be slaved to these parameters. In this mode, the VIRUS and LRS2 data acquisition systems must communicate to coordinate shutter open and close times, CCD read-out, and dithering (if required to fill the VIRUS field). While this operational mode can complicate the data acquisition and reduction for LRS2, it is a powerful method of maximizing the time-efficiency and scientific output of the HET.

LRS2-B and LRS2-R operate in unison as a subsystem of the entire upgraded HET observatory despite being optically independent instruments. In normal operations, LRS2 has multiple observing modes depending on the size of the source being observed and the desired wavelength range of the observations, as illustrated in Fig. $8b-d$. Point sources or small objects represent the simplest case where sky subtraction is provided in-situ by IFU spatial elements containing no object flux (Fig. 8*b*). For extended targets where the object fills the IFU, nodding the telescope off-source will be required to obtain sky spectra (Fig. 8*c*). When the observer needs data over the total range of wavelengths spanned by LRS2-B *and* LRS2-R together, "beam-switching" the two FOVs between the science target and a blank-sky field is utilized for objects that are $\lesssim 100''$ in size (Fig. 8*d*). For extremely large objects that are $\gtrsim 100''$ in size for which a small region of spectra is needed (e.g., the nucleus of a large, nearby spiral galaxy), the separation between the two LRS2 IFUs may not be large enough for the beam-switching method to be used for sky subtraction (i.e., after displacing the telescope, the first IFU may not be positioned over blank sky). In this case, separate observations and subsequent sky nods will have to be carried out for each LRS2 spectrograph pair individually.

Calibrations for the LRS2 science data include standard overscan correction, bias correction, dark correction, flat field correction, wavelength calibration, telluric correction, and flux calibration. For calibrations not from an astronomical source or the sky, the necessary calibration lamps are provided within the PFIP by the Facility Calibration Unit,[36] which is a deployable optical assembly that mimics the illumination pattern of the HET primary mirror and injects suitable calibration light into the WFC for obtaining flat fields and wavelength calibration for any of the HET facility instruments.

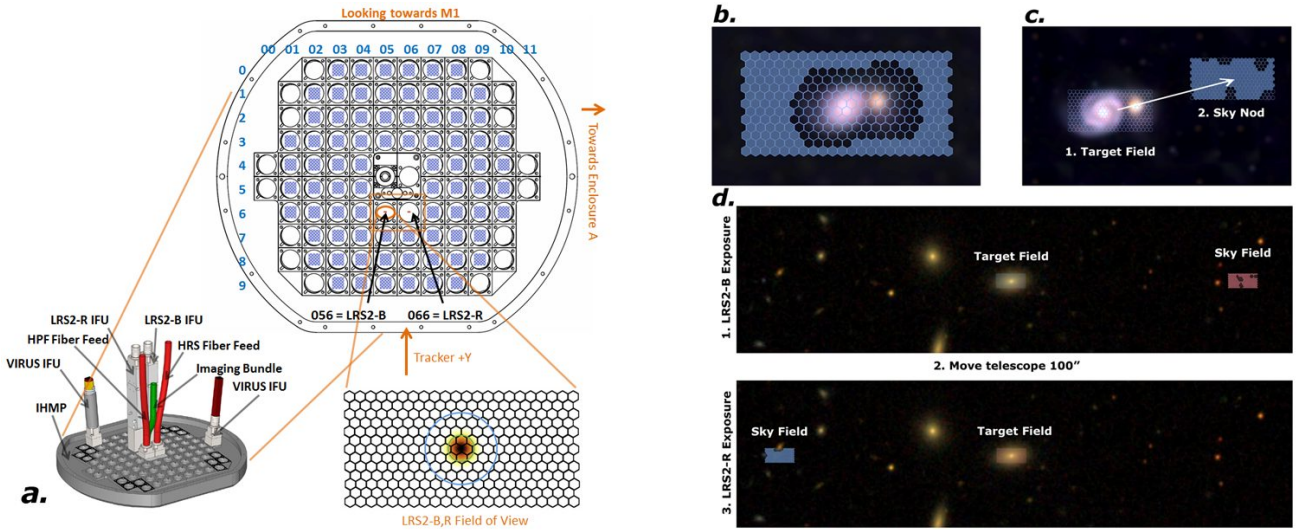

Figure 8. *a*) The configuration of the HET IHMP, onto which all of the HET facility instrument fiber feeds are mounted. LRS2's two fiber inputs are mounted 100″ apart near the center of the IHMP. Panels $b-d$ illustrate the LRS2 observing mode for obtaining sky background spectra, which depends on the size of the object and the desired wavelength coverage (see Sec. 3.7). Shaded spaxels are those that are suitable for sky measurements.

The above operations are conducted through the HET queue scheduling system.[9] The main operational change between LRS2 and the first generation LRS instrument is from slit spectroscopy to IFU observations. The IFU, in addition to the improved metrology provided through the HET WFU,[37] should reduce target acquisition to ~ 1 minute from the previous value of $\sim 10-15$ minutes. As a highly integrated subsystem of the HET, the operation of LRS2 is expected to be extremely reliable and efficient.

A data reduction pipeline based on the "CURE"[38] software package that has been developed for VIRUS will exist specifically for reducing the LRS2 integral field data. Similar to the adaptation of the VIRUS hardware, the implementation of CURE for LRS2 only requires minor adaptation to account for the different spectral data format. The pipeline will provide basic reduction and calibration of the data cubes and provide sky subtraction routines that are tailored to the types of expected targets.

4. ASSEMBLY & CHARACTERIZATION

4.1 VPH Grisms

Syzygy Optics, LLC was selected as the contractor to fabricate and assemble the four VPH grisms for LRS2. The physical dimensions of the grism assemblies were verified using a FaroArm Quantum portable contact coordinate measuring machine, and were found to be within tolerable variation about the nominal design.

External diffraction efficiency measurements were conducted using the same general-purpose grating test facility[39,40] that was developed to perform full characterizations of prototype VPH gratings for VIRUS. Several modifications to this test bench were required since it was not originally designed to test transmissive dispersing elements with non-plane-parallel substrates. The LRS2-B Orange Arm grism is shown under test in Fig. 9*a*. Multiple subapertures of the grism's clear aperture can be measured for characterization of the diffraction efficiency spatial variations that are caused by nonuniformities in the thickness of the DCG diffracting layer.[21] The measured external diffraction efficiency of the four LRS2 grisms was shown along with the RCWA predictions of the nominal design efficiency in Fig. 5*b*. Except for at the shortest wavelengths of the UV Arm, all four grisms are excellent and outperform the minimum external diffraction efficiency specification.

Prior to installing the grisms into the collimator assemblies, the critical dimensions of each assembled mounting cell were verified using the FaroArm. The measurements confirmed that the assembled mounting cells will sufficiently position the grisms within the specified tolerance. The grisms are bonded into the top assembly

Figure 9. Photos of the LRS2 collimator assembly. *a*) The LRS2-B Orange Arm grism under test using the VPH grating test bench that was originally developed for VIRUS. *b*) The LRS2-R Red Arm (right) and Far Red Arm (left) grisms installed into their fully assembled mounting cells. *c*) LRS2-B's collimator assembly complete, with the plastic cover removed to reveal the internal optics. *d*) Arrowed is one of the collimator vee-block shims that are used to fine-tune the camera-collimator angle to compensate for the delivered G_Λ values of the grisms.

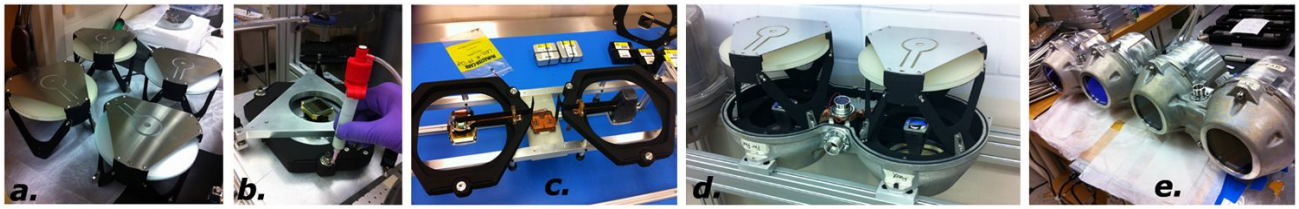

Figure 10. Photos of the LRS2 camera assembly. *a*) The four LRS2 camera mirror assemblies awaiting installation into the cryostat. *b*) Installation of bushings into the spider after alignment of the CCD detector. *c*) Installation of the cryogenic and detector electrical components onto the spider assemblies. *d*) Integration of the camera subassemblies into the cryostat. *e*) The two completed LRS2 camera assemblies prior to integration with the collimators (LRS2-R at left, LRS2-B at right).

using Dow Corning® 7091 Adhesive/Sealant, which has a strong but flexible bond and is well-suited for bonding materials with differing coefficients of thermal expansion (such as glass and aluminum). Photos of the completed grism assemblies are shown in Fig. 9*b*.

Due to having an oversized photodiode detector to ensure that all flux is measured for diffraction efficiency testing, the VPH grating test bench described above can only verify the diffraction angles to within $\pm 0.5°$ (± 90 pixels on the LRS2 CCD). To avoid wasting detector space within the dichroic cross-over regions, knowing a precise delivered value of grism dispersion is necessary so that the resulting wavelength bounds for each spectrograph channel can be accurately determined. If these wavelength bounds are unsatisfactory relative to the dichroic transition wavelength, some degree of corrective action can be taken prior to the final optical alignment. After the spectrographs were fully assembled and a preliminary optical alignment was completed (see below), the IFU was illuminated with an appropriate emission line lamp, and the focal plane data was compared to Zemax optical models. A measurement of the locations of emission lines in the spectral direction suggested that the dispersion assumed in the optical models was incorrect, and that the laboratory measured G_Λ values of the grisms were systematically smaller than the specification by ~ 6 lines mm^{-1}. For the UV, Orange, Red, and Far Red Arms, measured values of G_Λ are 1764, 770, 918, and 792 lines mm^{-1}, respectively.

4.2 Collimators

With the exception of the grism installation, the procedures[33,41] for assembling the LRS2 collimators are identical to VIRUS. Once the fold mirrors, collimator mirrors, and grisms are properly installed into their respective mechanical mounts, the assembly of a kit of collimator components takes less than one hour to complete. The position of the collimator mirror is set close to its nominal position in tip/tilt and focus relative to the back of the collimator baseplate using a set of precision machined fiducial spacers. Fig. 9*c* shows the assembled LRS2-B collimator.

Figure 11. Assembly of the LRS2 IFU inputs. *a*) Feeding fibers through the hole block by Berlin-Fibre GmbH. *b*) The LRS2-B input heads. The nickel is shown for scale. Individual lenslets can be seen. *c*) The focal extender subassembly. Doublet 2 can be seen protruding from the end of the lens barrel. *d*) The dichroic subassembly housing. *e*) A fully assembled LRS2 IFU input assembly.

The reduced fringe frequencies of the grisms described in the previous section results in a smaller angle of diffraction for a given angle of incidence, which means that the wavelength bounds for each spectrograph channel will be redder than the nominal design. This was partially compensated for by adding shims of the proper thickness under the appropriate kinematic vee-block mounts to which the camera mates on the rear side of the collimator's baseplate (see Fig. 9*d*). For LRS2-B (LRS2-R), shims with a thickness of 2.655 mm (1.770 mm) were fabricated and installed under the upper two vee-block mounts to make the angle between the collimator and camera 0.6° (0.4°) shallower than the nominal value of 24.3°. The change in dispersion also results in a slight increase in wavelength coverage for each channel. Since the Far Red Arm's instrumental throughput very quickly falls off due to the poor sensitivity of the CCD detector at long wavelengths, the camera shims for LRS2-R were designed to add this small increase in wavelength coverage to the blue side of the Red Arm. A shallower angle for the LRS2-B camera allows the additional wavelength coverage to extend further into the near-UV, rather than further into the redder wavelengths of the Orange Arm since that spectral regime is already efficiently covered by the LRS2-R Red Arm.

4.3 Cameras

With the exception of the exchange of a number of components that are custom to LRS2, the assembly of the LRS2 cameras follows an identical process[42,43] to that established for VIRUS. The camera mirrors are not preset to a specific tip/tilt or focus position prior to the optical alignment of the instrument.

To proceed with alignment, the camera is sealed using a temporary "adjuster back" that allows mechanical and visual access to the camera mirror adjustment and locking set screws while the cryostat is under vacuum and the detectors are cold. During lab characterization and actual usage of LRS2, a standard camera cryostat cover that blocks access to these adjustment screws and is outfitted with the vacuum measurement and maintenance instrumentation is utilized. After the assembly is complete, the camera assembly is mated with the collimator assembly. This is done very repeatably by utilizing the set of three kinematic vee-blocks that are mounted to the rear of the collimator baseplate inside of which a set of matching tooling balls that are mounted on the front of the camera cryostat rest. Photos of the LRS2 camera assembly is shown in Fig. 10.

4.4 Integral Field Units & Input Feed Assemblies

As described in Sec. 3.3.1, each LRS2 spectrograph pair uses the well-established VIRUS IFU cable design. The construction of the two LRS2 IFU cables was completed by Berlin-Fibre GmbH using the facilities at Leibniz-Institute for Astrophysics Potsdam that were setup for VIRUS IFU and fiber cable production (see Fig. 11*a*). University of Texas at Austin personnel completed the alignment and installation of the double-stack of microlens arrays for each of the four IFU input heads (see Fig. 11*b*). For details on the construction of the output heads, the reader is referred to Ref. 26.

After the fiber cables are constructed, the assemblies are shipped from Germany to The University of Texas at Austin where the remainder of the construction of the input feed optics assembly is completed. To complete the assembly, three parallel steps are carried out before the integration of the IFUs, as illustrated in Fig. 11$b-d$, respectively. First, to complete the assembly of the input heads, the two field lenses (one for each input head)

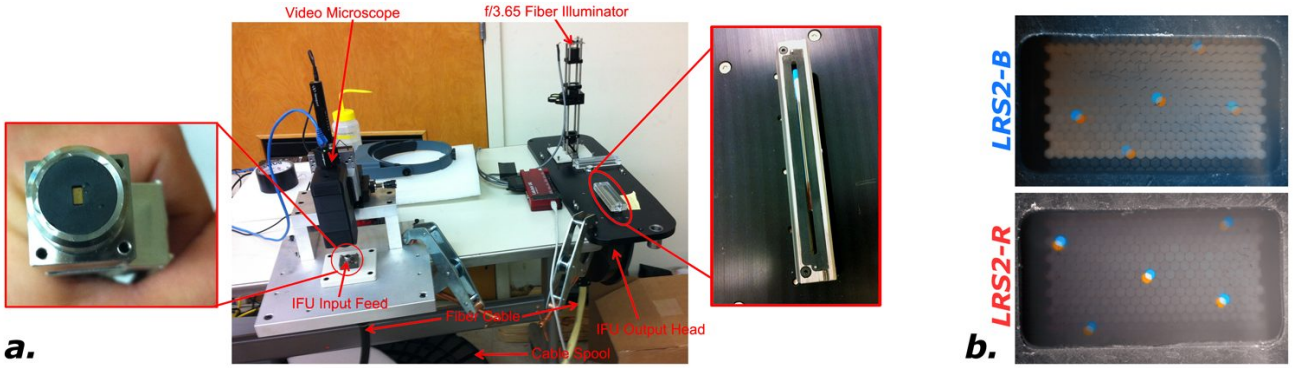

Figure 12. *a*) The test setup used to characterize the LRS2 IFUs. Major components are labeled. A close-up view of the input end of one of the LRS2 IFUs is seen at left, while a close-up view of a fiber slit at the output can be seen at right. *b*) The measured registration error of the two channels for LRS2-B (top) and LRS2-R (bottom). The illuminated spaxels in the bluer channel for each spectrograph pair are shown in blue, the redder channel spaxels are shown in Orange, and the fully back illuminated microlens arrays can be seen in gray.

are glued over the top of the microlens arrays. No specialized fixturing is required for this installation. A second parallel step is the assembly of the focal extender subassembly, which consists of the installation of the two doublet lenses and the knife-edge pupil baffle. The order blocking filter is also installed behind the baffle for LRS2-R only. Doublet 1 (see Fig. 3*a*) is first installed, and is glued into a precision positioning pocket that is machined into the lens barrel housing (which is also made from stainless steel). After the baffle is epoxied into place within the lens barrel, Doublet 2 is installed on the opposite end in the same manner as for Doublet 1. The third parallel step is the installation of the dichroic and fold mirror into the dichroic subassembly housing. The housing sleeve is made of stainless steel and was precisely fabricated using wire EDM.

The fiber cable and the input feed optics assemblies are then integrated. The IFU input heads are integrated directly into the mechanical sleeve inside of which the dichroic and fold mirror are mounted. M1 locating pins are inserted into holes on the side of the sleeve on which the front of the input head assemblies rest to set their rough focus position. Once the input heads are seated on these pins, a series of 8 set screws are tightened to force the input heads against the precision machined perpendicular inner walls of the sleeve. The fiber cable is then fastened to the top of the dichroic subassembly. Furthermore, a cylindrical positioning feature on the end of the focal extender subassembly is inserted into the end of the dichroic subassembly, and clamped into place to complete the integration of the IFU feed optics assembly. A fully assembled IFU input head can be seen in Fig. 11*e*.

For conducting system tests of the fully assembled IFUs (see Fig. 12*a*), a video microscope is used to image the focal surface of the system input that is formed at the end of the focal extender assembly lens barrel. Individual fibers are back-illuminated from the output end with light that is within each spectrograph channel's respective passband at $f/3.65$, which forms an image of the illuminated lenslet at the input end. To aid in stray light control, an aperture mask is installed at the end of the focal extender lens barrel coincident with the focal surface. The aperture measures 2.75 mm $\times$ 1.44 mm, which is oversized by $\sim 20\%$.

Prior to integration with the assembled LRS2 spectrographs, the IFU fiber mapping was verified, and the focus was evaluated for each channel in each IFU relative to each other and relative to the input aperture mask that is coincident with the nominal focal surface. The degree of measurable focus gradients across each channel's focal surface indicated good axial alignment of the input heads relative to the macroscopic optics in the focal extender. Finally, a measurement of the registration error between the two channels at the input focal plane is made. As long as the registration error is well-measured and is within a single lenslet pitch, it is possible to interpolate the results of one channel's field to the spaxel coordinates of the other channel, if necessary. To make this measurement, the same five individual fibers were back-illuminated on both of the channel's fiber slits. The location of these illuminated fibers at the input were then measured with the video microscope in both channels. For LRS2-B, the translational error between the UV and Orange Arms is 0.50 ± 0.03 times the lenslet pitch

(i.e., $0.30'' \pm 0.02''$ on sky), while the rotational error and magnification difference is constrained to $< 0.3°$ and $< 0.5\%$, respectively. The measurements for LRS2-R are very similar to LRS2-B, and are 0.49 ± 0.04 times the lenslet pitch, $< 0.3°$, and $< 0.5\%$, respectively. The registration error is visualized using data taken with the video microscope in Fig. 12*b*.

As a final step to verifying the LRS2 IFU assembly, the efficiency was measured relative to a well-characterized VIRUS production IFU by taking back-to-back measurements of stable emission line lamps with each IFU attached to the aligned LRS2 spectrograph pair (see below). The ratio of the flux in images of the same emission line taken with the VIRUS IFU to that taken with the LRS2 IFU was calculated and subsequently corrected for known differences in the fiber aperture size, fiber cable length, and attenuation in the high-OH fibers used in the VIRUS IFU due to combination vibrations in the hydroxyl species[44] contained within the glass. Once the efficiency of the LRS2 IFU feed optics are taken into account, the absolute coupling efficiency can be derived. For the UV, Orange, Red, and Far Red Arms, the derived coupling efficiency averaged over the channel wavelength range is 58.2%, 79.8%, 80.7%, and 86.9%, respectively, compared to the expectation of 90% from the optical models of the design. It is not yet understood why the UV Arm's coupling efficiency is significantly lower than both the expected coupling efficiency and the measurements for the other three channels.

4.5 Spectrograph Optical Alignment

Utilizing VIRUS assembly standards[33,41–43] for the camera and collimator assemblies, the majority of the optical components in the spectrographs are aligned *during* construction. The only degrees of freedom for optical compensation[45] that are required to reach the optimal plate scale and full-field focus are the tip, tilt, and piston of the camera and collimator mirrors. Once aligned, the LRS2 spectrographs do not require further adjustment when deployed due to the athermal optomechanical design and operation in a constant gravity vector.

4.5.1 Laboratory Configuration

Existing lab facilities that were established for VIRUS optical alignment and characterization were also utilized for LRS2, as shown in Fig. 13*a*. All alignment tasks are carried out with the camera cryostats under vacuum and cooled to operational temperature ($-110°$ C). Cooling of the detectors in the lab is achieved with a custom cryogenic header tank that terminates at the camera's cryogenic bayonet via a gravity fed vacuum-jacketed line. For optical alignment, the CCDs are controlled using a production VIRUS CCD controller that has been modified to operate alone without the full multiplexed VIRUS detector system working around it.

A suite of emission line and continuum calibration lamps is housed inside of a simple aluminum enclosure which acts to diffuse the calibration light. The scattered light from the lamps is directed into a controlled range of angles by an engineered diffuser, and is further fed to the fibers at the IFU input head by a series of lenses that come to a focus at the proper $f/3.65$ focal ratio. Prior to the diffuser, the system is shuttered by an off-the-shelf shutter that is triggered through a direct connection to the CCD controller. To cover the full spectral range of LRS2, emission line calibration lamps include mercury-argon (Hg), cadmium (Cd), argon (Ar), neon (Ne), and krypton (Kr). Continuum sources include deuterium and quartz tungsten halogen (QTH) lamps.

For collimator mirror adjustment, a set of three micrometers with 10 μm resolution ($\sim 15''$ in tip/tilt) are threaded into the collimator baseplate and push against the back of the collimator mirror support plate, which is preloaded with springs that are set on the Invar metering rods. Once alignment of the collimator mirror is achieved, the support plate can be locked down on the metering rods, and the micrometers can be removed from the baseplate.

Since the camera must be under vacuum for the detectors to be cooled during optical alignment, camera mirror adjustment is achieved using a custom "adjuster back" cryostat cover that features three ferrofluidic vacuum feed-throughs and vacuum windows for each camera mirror for accessing the mirror adjustment and locking screws. Each hex key feed-through has a dial indicator, which combined with the M4×0.7 mm adjustment set screws yields a 2 μm resolution in focus ($2''$ in tip/tilt). Considering backlash in the system, these values are realistically larger by a factor of a few.

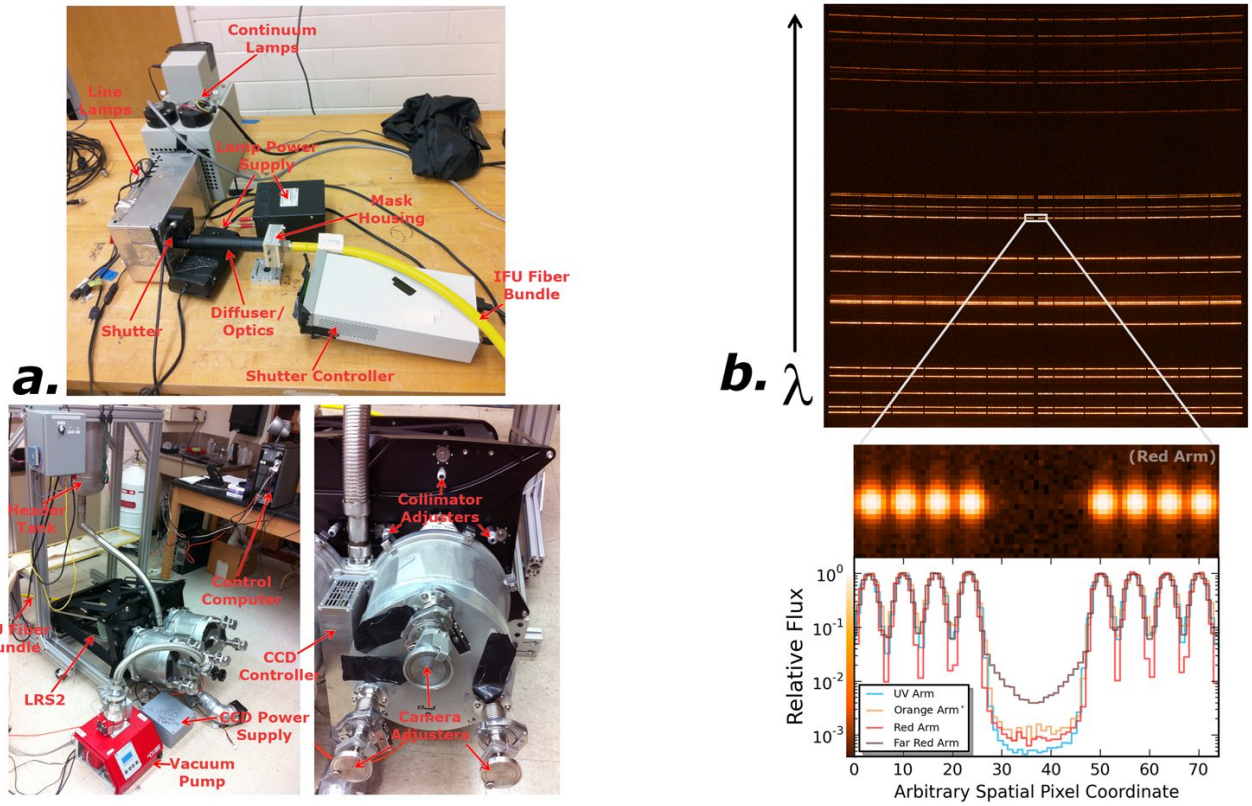

Figure 13. *a*) The optical alignment setup for LRS2. The top photo shows the light sources coupled to the VIRUS alignment IFU that was used for first-order alignment. The lower left photo shows the LRS2-B spectrograph during the alignment process. The lower right photo shows a close-up of the adjuster knobs on the back of the collimator and the camera "adjuster back". *b*) An illustration of the aligned LRS2 image quality. A Ne emission line spectrum taken with the Red Arm is shown, and the zoomed-in inset shows a subset of fibers near the center of the chip across which fiber profiles are shown for each LRS2 channel.

4.5.2 First-order Alignment

In the VIRUS/LRS2 optical design, tip/tilt and focus adjustments of the camera and collimator mirrors are degenerate to first-order in terms of their effect on the focal plane image quality and image position. However, the magnification of the dispersed fiber images can be fine-tuned by adjusting the camera mirror focus and compensating with the collimator mirror piston to bring the images back to focus (or vice-versa). Thus, by measuring the distance in the spatial dimension between separate fiber images on the detector, one can constrain the unique focus positions of each mirror. To decouple the tip/tilt adjustments and optimize the final image quality, an in-situ full-field moment-based wavefront sensing technique was developed for efficient alignment of VIRUS units.[46] This method provides deterministic alignment corrections based on the geometric relation between the calculated image shape moments for focus-modulated images and the wave aberration coefficients. For VIRUS, evenly spaced fiber images on the focal plane are provided by an Hg+Cd emission line lamp combination that sparsely illuminates the IFU.

Due to limited resources, the software for implementing the full-field moment-based wavefront sensing technique was not modified to work with LRS2's different spectral and spatial format. However, the technique was implemented for a first-order alignment of the camera and collimator mirrors by reconfiguring each LRS2 channel with a VIRUS IFU, a VIRUS diffraction grating, and by removing the camera mounting shims. For the two LRS2-B channels that are reconfigured in this way, the VIRUS full-field moment-based wavefront sensing software is directly implemented to calculate the required camera and collimator mirror adjustments. The result-

ing image quality is excellent, and the camera mirrors are subsequently locked in place leaving only collimator tip/tilt and focus adjustments available for final image quality optimization. Worse results were achieved for the LRS2-R channels in the VIRUS configuration because the optical prescription of the field flatteners and corrector plates are different from VIRUS. While the focus corrections for LRS2-R are acceptable to first-order, the camera mirrors remain unlocked to provide more flexibility in the final alignment steps described below. Once the corrections to the collimator and camera mirrors from the full-field moment-based wavefront sensing technique are applied, the LRS2 spectrographs are reconfigured with their respective grisms, camera mounting shims, and IFUs for final adjustment, as described below.

4.5.3 Final Alignment with the LRS2 IFU

For the final alignment and laboratory characterization of the integrated LRS2 system, the LRS2 IFU input head is mated to the same diffuser and fore-optics assembly that was used with the VIRUS alignment IFU to feed the system at $f/3.65$ with calibration light, as described in Sec. 4.5.1. The first step in the final alignment procedure of LRS2 is to align the grism so that the fiber images are centered between the two amplifier regions of the CCD detector, after which the grism mount rotation stage is locked down. After the first-order alignment described above, the image quality is quite close to optimal. However, due to the dispersion of the grisms being delivered out-of-specification as discussed in Sec. 4.1, the wavelength bounds on the edge of the detectors are not as specified and a larger portion of the low throughput dichroic overlap region is imaged on the chip. The shims that were added behind the camera mounting vee-blocks help to recover useful spectra on the detector by changing the camera-collimator angle. However, an additional small tip adjustment of the collimator mirror is required to recover the optimal wavelength bounds within the cross-over region.

While the required collimator mirror tip adjustments are small enough for each channel to ensure that the collimated beam is not translated out of the clear aperture of the grism, they are large enough to induce a small but measurable change in the image quality. To compensate, the collimator mirror is actuated through ± 300 μm of focus in several equally spaced steps on either side of the initial position. The image quality of the emission line images at each focus step are analyzed visually across the detector for asymmetries or softness. Image quality is quantified in several locations across the CCD detector by calculating the "contrast" metric, which is defined by:

$$\text{Contrast} \;=\; (I_{\text{peak}} \;-\; I_{\text{valley}}) \;/\; (I_{\text{peak}} \;+\; I_{\text{valley}}) \;. \tag{1}$$

Here, I_{peak} and I_{valley} are the background-subtracted pixel intensities (in analog-to-digital units; ADUs) at the peak of the fiber image and in the valley between the fiber and its neighbor, respectively. Note that for VIRUS, the image quality specification[3] requires that $\geq 90\%$ of the fiber images across the detector have a contrast of ≥ 0.6. The collimator is actuated to the focus position that yields the best overall image quality as evaluated by these methods, and is subsequently locked in place to complete the optical alignment.

In Fig. 13*b*, a background-subtracted image of Ne emission lines are shown for the LRS2-R Red Arm, along with a cross cut of the background-subtracted emission line spectra near the center of the detector for each LRS2 channel. Each channel displays excellent separation between adjacent fibers and very similarly shaped fiber core images. A more rigorous determination of the overall image quality is performed by illuminating the IFU with a continuum source. The background-subtracted continuum image is coadded in 4 pixel-wide bins in the spectral direction, which roughly corresponds to the size of the fiber core image on the LRS2 detector. For each bin across the detector, the contrast was calculated for all 280 fibers on the IFU. In Fig. 14*a*, the empirical cumulative distribution function (ECDF) of contrast measurements for each LRS2 channel is shown compared to a similar measurement made for a sample of fully-aligned VIRUS units. This figure illustrates that after the initial optical alignment, the image quality of the UV, Orange, and Red Arms are all at least as good as or better than fully-aligned VIRUS channels. The 50% cumulative fraction corresponds to contrasts of 0.805, 0.805, and 0.929, respectively. The ECDF for the Far Red Arm, however, appears to suggest poorer image quality. Despite this, visual inspection of the shapes of the fiber core images (e.g., Fig. 13*b*) across the entire Far Red Arm detector are comparable to the other channels. Upon further inspection, it was found that the Far Red Arm's ECDF is being biased by scattered light, which is further described in Sec. 4.6.3. Despite the extended tail of low contrast values, the delivered image quality of the Far Red Arm is otherwise good with a 50% cumulative fraction corresponding to a contrast of 0.785. Spectral resolution measurements presented below in Sec. 4.6.2 also validate that the Far Red image quality is acceptable, sans the scattered light.

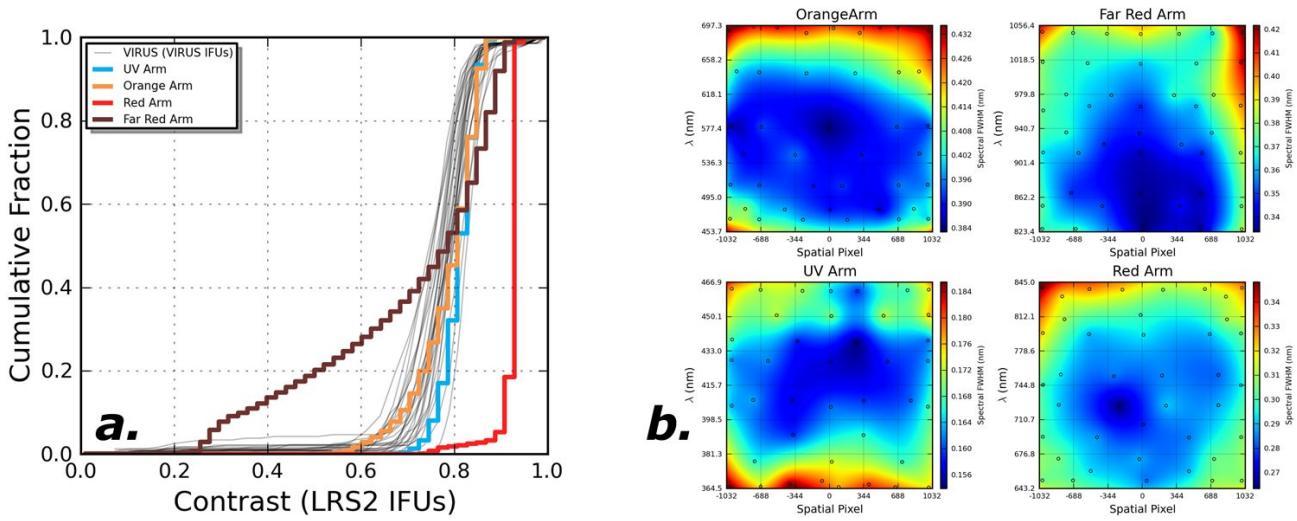

Figure 14. *a*) Contrast ECDFs for each LRS2 channel after the final alignment procedure. The gray ECDFs are examples from aligned VIRUS channels for comparison. *b*) Maps of the FWHM spectral resolution $\delta\lambda$ for each LRS2 channel.

4.6 Laboratory Characterization

For performance characterization, the aligned LRS2 spectrograph pairs are placed into the final hardware configuration as they will be delivered to the telescope. This includes installing a baffle in between the two channels within the collimator, installing the light-tight collimator cover, and replacing the camera adjuster back with the standard camera cryostat cover that is outfitted with the vacuum instrumentation assembly.

4.6.1 Vacuum and Cryogenic Performance

Before the LRS2 camera is connected to the cryogenic system, it is pumped down to a pressure of $\lesssim 10^{-4}$ Torr. The cryogenic bayonet is then attached to the camera. As the activated charcoal getter cools, the pressure in the cryostat drops further due to cryogenic trapping. Once the vacuum valve is closed and the turbo pump is removed from the system, the ion pump is switched on. The vacuum characterization tasks described here took place over approximately two weeks for each spectrograph. The ion pump and vacuum gauge remained on as long as test images were not being taken with the spectrograph, since each of these devices are capable of emitting low levels of optical radiation while in operation. With the ion pump off, the initial steady-state pressure was 1.6×10^{-6} Torr for LRS2-B and 1.1×10^{-6} Torr for LRS2-R. With the ion pump on, the pressure is typically a factor of ~ 2 lower (8.3×10^{-7} Torr for LRS2-B and 7.9×10^{-7} Torr for LRS2-R, initially). Pressure measurements in both states of the ion pump were usually taken once per day. With the ion pump on, the pressure steadily increased by 4.6×10^{-8} Torr day^{-1} for LRS2-B and 1.1×10^{-8} Torr day^{-1} for LRS2-R. Under the assumption that the increase in the pressure remains linear with time, it is estimated that the pressure with the ion pump on (off) will be 1.8×10^{-5} Torr (3.8×10^{-5} Torr) for LRS2-B and 4.7×10^{-6} Torr (2.8×10^{-5} Torr) for LRS2-R after one full year of operation without intervention. Under these conditions, the recorded equilibrium temperature under closed-loop control for each LRS2 channel is safely under the specified operational temperature regulation setpoint of -110 ° C.

4.6.2 Image Quality and Spectral Resolution

The contrast ECDFs presented above primarily quantify the spectrograph's ability to separate adjacent fiber images in the spatial dimension. To quantify the image quality in the spectral dimension (which provides a measurement of the delivered spectral resolution), images were taken with emission line lamps and Gaussian functions were fit to unblended emission lines across each channel's detector after the individual fiber images were collapsed spatially along their width. In units of pixels, the average (standard deviation) full width at half maximum (FWHM) measurements for the UV, Orange, Red, and Far Red Arms are 3.38 (0.16), 3.46 (0.17), 3.07 (0.16), and 3.25 (0.18), respectively. For each channel, the delivered image quality is excellent, so much so

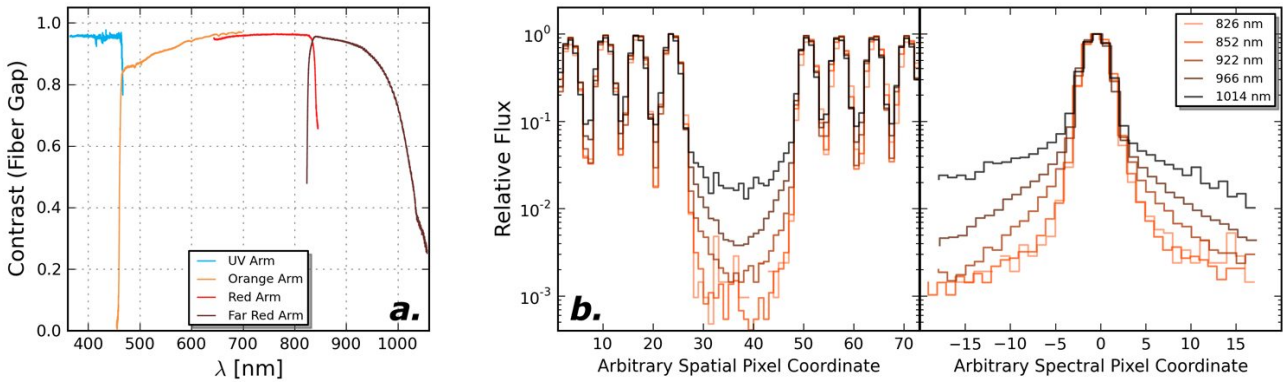

Figure 15. Stray light measurements for LRS2. *a*) The scattered contrast as a function of wavelength for each channel, which illustrates the amount of light scattered by a given fiber into the adjacent fiber. *b*) Spatial (left) and spectral (right) fiber profiles of Ar emission lines in the Far Red Arm, which shows an increase in the strength of the point spread function wings beyond 922 nm. The wings in the spectral profile are similar in strength to the relative flux levels in the trough of the spatial cut. Since there is no overlap in profiles in the spectral cut, this suggests that scattering is stronger in the spectral dimension.

that binning of the CCD detector pixels will undersample the fiber image. As a result, LRS2 should always be operated in 1×1 CCD binning mode.

For each LRS2 channel, a wavelength solution was determined for the central fibers by fitting a third order polynomial to the pixel locations of $\sim$ 10 emission lines. The 1σ residual of these wavelength solutions are typically $\sim$ 0.1 Å. Using the wavelengths that fall on the first ($\lambda_{\rm min}$) and last ($\lambda_{\rm max}$) pixel of each LRS2 CCD detector, the linear dispersion P for 1×1 CCD binning is calculated as $(\lambda_{\rm max} - \lambda_{\rm min})/2064$. Using these linear dispersion measurements, the FWHM measurements above are converted into wavelength units. Fig. 14*b* shows maps of the resulting FWHM spectral resolution $\delta\lambda$ for each channel. Using the central wavelength on the detector divided by the average value of $\delta\lambda$, the delivered spectral resolving power R for each LRS2 channel is 2474, 1427, 2480, and 2561 for the UV, Orange, Red, and Far Red Arms, respectively. These optical system-level properties are tabulated in Table 4.

4.6.3 Stray Light

The LRS2 optical system is generally quite free of stray light, ghost images, and scattered light. The fiber profiles shown in Fig. 13*b*, which cut through one of the gaps between the fiber banks in the IFU output slit, shows the amount of light that is scattered into a fiber trace from adjacent fibers. The UV, Orange, and Red Arms show very low levels of scattered light that is nearly three orders of magnitude below the peak flux in the fiber images. The exception to this is the Far Red Arm, which shows a little more than one order of magnitude difference between the peak flux in the fiber images and the trough of the fiber gap.

Property	UV	Orange	Red	Far Red
λ_{min}	364.4 nm	453.7 nm	643.2 nm	823.4 nm
λ_{max}	466.8 nm	699.7 nm	845.0 nm	1056.4 nm
Linear Dispersion *P*	0.496 Å px^{-1}	1.192 Å px^{-1}	0.978 Å px^{-1}	1.129 Å px^{-1}
Mean Spectral Resolution $\delta\lambda$	1.68 Å	4.04 Å	3.00 Å	3.67 Å
Mean Resolving Power *R*	2474	1427	2480	2561
Contrast (50% cumulative)	0.81	0.81	0.93	0.79
Mean Scattered Contrast	0.95	0.90	0.95	0.80

Table 4. Optical system-level properties of the LRS2 spectrograph channels.

The evaluate the amount of light that is scattered into a fiber trace by an adjacent fiber as a function of wavelength, a one-dimensional (1-D) spectrum is extracted from a fiber that is adjacent to one of the gaps, where the pixel values are summed in the spatial dimension over the width of the fiber. The same extraction procedure is followed by moving the extraction window into the fiber gap where a fiber would otherwise be. At each pixel in the spectral dimension, the contrast (see Equation 1) is calculated, where $I_{\rm peak}$ is the value of the 1-D spectrum for the fiber and $I_{\rm valley}$ is the 1-D "spectrum" extracted from the fiber gap. The scattered contrast is shown as a function of wavelength in Fig. 15*a*. For the UV, Orange, and Red Arms, the scattered light contrast measurements are generally excellent at > 0.85.

The Far Red Arm shows excellent scattering characteristics below 950 nm, but features a steep decline for longer wavelengths, which is the inverse of what is expected for surface scattering. This increase in scattered light is the cause for the long low contrast tail in the ECDFs shown in Fig. 14*a*. To further investigate the Far Red Arm scattering, cross cuts across the central IFU slit gap for five Ar emission lines spread across the wavelength range of the channel are shown in 15*b*. These plots show a marked increase in the scattered light at relatively large distances from the peak image flux starting at 922 nm. While the increased scattering can be seen in both the spectral and spatial profiles, it is stronger in the spectral dimension. The cause of this scattered light is the continued subject of investigation.

4.6.4 Detector Characterization

Characterization[47] of the LRS2 detectors is performed using the same methods as VIRUS, which are primarily based on measuring sets of flat field images taken at various illumination levels to populate a photon transfer curve.[48] This analysis yields the detector read noise, system gain, linearity, and full well capacity. For detector characterization using the dedicated LRS2 detector system electronics and data acquisition software, continuous flat field images are obtained by replacing the standard IFU with a custom "continuous slit output head" that was developed for VIRUS characterization. The continuous slit output head consists of a large B270 glass plate, with one end fine ground and the other polished. A large numerical aperture liquid light guide is coupled to the polished end of the glass plate on one end, and is fed by a broadband source at the other. The light traverses the plate from the liquid light guide and illuminates the fine ground edge that is placed at the back of the slot in the spectrograph fold mirrors where the fiber slit of the standard IFU output head would sit. Combined with a smooth, broadband source, the result is a continuous illumination of the detector in the spatial and spectral dimensions. Additional properties of the detectors were measured by the vendor (The University of Arizona Imaging Technology Laboratory; ITL). ITL measured the LRS2 CCD detectors to have linearity residuals at the $\lesssim 0.2\%$ level, and charge transfer efficiencies of ≥ 0.999995. The ITL-measured QEs are plotted and the measured properties of the detectors are tabulated in Fig. 16. Significant sensitivity and uniformity degradation have been observed in a large number of the VIRUS detectors, so the QEs reported in Fig. 16 may not be representative of the actual performance of the LRS2-B CCD detectors. For more information, see Ref. 3. The LRS2-R detectors appear to be much more robust, and have not displayed any susceptibility to such uniformity degradation.

5. ON-SKY PERFORMANCE

5.1 Deployment

By utilizing the VIRUS design, LRS2 takes advantage of the new HET infrastructure that supports the VIRUS spectrograph array. LRS2-B and LRS2-R are rack mounted inside one of the large environmentally controlled VIRUS enclosures[49] that are mounted to the sides of the HET telescope truss structure. As can be seen in Fig. 17*a*, the LRS2 spectrographs are located in the top-corner of the enclosure in bays A11 (LRS2-B) and A21 (LRS2-R), which are the closest positions to the fiber cable strain relief to minimize the fiber cable length and maximize the instrumental throughput. Additional infrastructure is added to these enclosure bays to support the LRS2 vacuum instrumentation subsystem, including racks for mounting the vacuum gauge and ion pump controllers, a remotely switched power distribution unit, and a serial device server and Ethernet lines for communication. As shown in Fig. 17*a*, the two LRS2 CCD controllers are powered from one of the VIRUS filter box and power supplies that are located in the large electronics rack annex in the lower corner of the enclosure. LRS2's dedicated

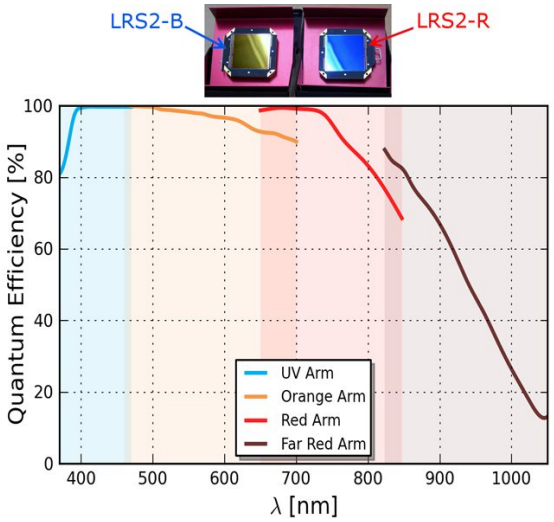

Property	UV	Orange	Red	Far Red
Read Noise	3.45 e-	3.50 e-	3.53 e-	3.63 e-
Gain	0.794 e- / ADU	0.813 e- / ADU	0.882 e- / ADU	0.873 e- / ADU
Full Well	>1.10x10^5 e-	>1.10x10^5 e-	>1.10x10^5 e-	>1.03x10^5 e-
Dynamic Range	>90.1 dB	>89.9 dB	>89.9 dB	>89.1 dB
Dark Current (at -110° C)	5.35x10^{-4} e-/px/s	1.10x10^{-3} e-/px/s	1.21x10^{-3} e-/px/s	5x10^{-4} e-/px/s
Linearity	Residuals better than 0.2%			
Charge Transfer Efficiency	>0.999995			

Figure 16. LRS2 CCD detector properties. At left is a plot of the QE as measured by ITL before delivery. At right is a table showing the basic measured properties of the four detectors. The read noise and gain values are from in-house characterization measurements using photon transfer. Other properties were also measured by ITL before delivery.

MUX unit is also located in this rack. The LRS2 Control Computer is located off of the telescope structure in a lower electronics room with the control computers for other instruments and HET subsystems.

The VIRUS support infrastructure also contains the extensive liquid nitrogen distribution system[50] that cools CCDs for the entire VIRUS array and for LRS2. At the top of each enclosure is a header tank which provides a continuous flow of cryogen to the various lateral levels of vacuum jacketed pipes for each row of spectrographs in each enclosure. The header tanks are replenished from a large external dewar, which is refilled by an 18-wheel tanker truck every two weeks. For each enclosure bay, a flexible hose terminates with the novel copper heat exchanger bayonet[51] that conducts heat out of the camera cryostat and allows the camera to be disconnected from the cryogenic system without affecting the rest of the system.

LRS2-R was deployed in November 2015, and was the first spectrograph to be installed on the newly upgraded HET. The deployment of LRS2-B followed in February 2016, along with several VIRUS spectrographs, at which time the official commissioning of the instrument commenced. Photos of the spectrograph deployment are shown in Fig. 17$b-e$. Installation of the spectrograph pairs into the fully commissioned VIRUS enclosure is a relatively simple procedure that requires a little more than an hour to complete. The most complicated aspect of the LRS2 (and VIRUS) deployments is the installation of the IFU input head on the IHMP, and the subsequent unraveling and cable routing of the fiber cable. This procedure requires at least a half dozen individuals distributed at various locations on the telescope to ensure the safety of the fiber cable, and to temporarily secure the input and output heads while the cable is attached to multiple strain relief connectors along its length. A photo of the two newly installed LRS2 spectrographs is shown in Fig. 17c, along with the fiber cable and HET WFC in the background.

5.2 Sensitivity Model Validation

First light with LRS2-R and LRS2-B was achieved on November 18, 2015, and February 10, 2016, respectively. Among the primary initial commissioning tasks was to verify the throughput models that were established during the engineering phase of the instrument's development. Initial predictions of the LRS2 system throughput were presented by Ref. 19, and were based on the throughput model used for VIRUS which has been verified against on-sky tests using the Mitchell Spectrograph.[22] The initial LRS2 throughput model was updated by Refs. 18 and 20 using available measurements of individual optical components, and is updated again here using the as-delivered efficiencies of the grisms and the measured coupling efficiencies of the IFUs. To be conservative, some level of FRD is assumed for the LRS2 IFU fibers such that 30% of the light is lost within the spectrograph due to

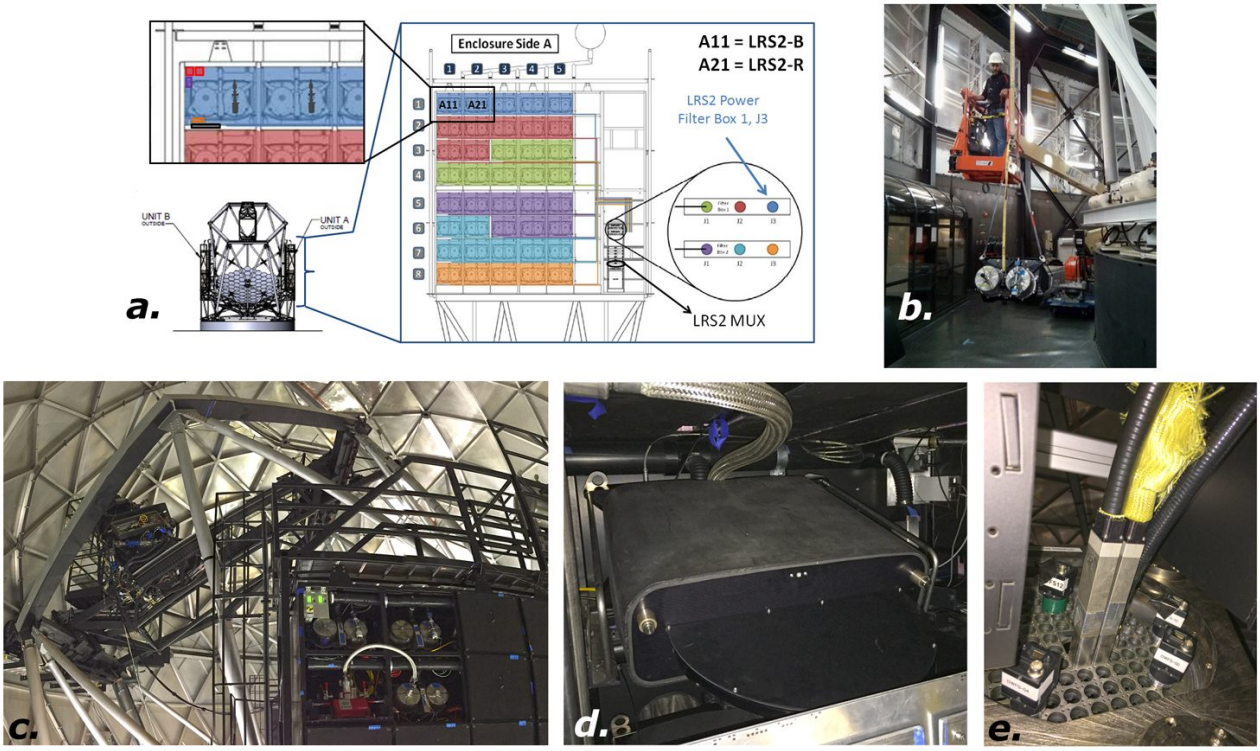

Figure 17. Deployment of the LRS2 spectrographs on the HET. *a*) A schematic view of the VIRUS enclosure layout into which the LRS2 spectrographs are installed. The location of the LRS2 vacuum gauge controller (purple), ion pump controllers (red), communication devices (orange), and PDU (black) are shown in the zoomed inset. The enclosure bays are color-coded according to where their power is connected. *b*) A photo of the author during the LRS2-R lift. *c*) The installed LRS2 spectrographs in the open VIRUS enclosure with the HET WFC in the background. A VIRUS unit and attached vacuum pump can be seen below LRS2. *d*) LRS2-R after installation seen from the IFU ouput head side of the VIRUS enclosure. *e*) The IHMP shown with the two LRS2 IFUs installed. A single VIRUS IFU can be seen installed behind LRS2. The small cameras are wavefront sensors for testing the WFC.

the geometric obstruction. Since measurements of the IFU FRD were not able to be made prior to deployment, this assumption is moderate and lies in between the ideal case of no FRD, and the case of extreme FRD resulting from damaged fibers that turn the exit pupil into a Gaussian distribution. Note that all throughput values are relative to 10 m diameter, fully-filled aperture at the top of the atmosphere.

Fig. 18*a* shows the expected total throughput of LRS2 both with and without the combined effect of the HET and the atmosphere. The calculation of the "HET + atmospheric" throughput takes into account the HET primary mirror reflectivity with coatings that are in a typical state of degradation, the expected throughput of the WFC, and the transmission of the atmosphere at an airmass of 1.22 (which is a typical value for the HET's fixed altitude design). Atmospheric extinction, Galactic extinction, and the mean illumination of the HET's primary mirror during a track are not accounted for in the model.

To provide a crude first measurement of the total system throughput, spectrophotometric standard stars BD+26 2606 and HD19445 were observed on February 13, 2016 and November 20, 2015 with exposure times of 120 seconds and 10 seconds for LRS2-B and LRS2-R, respectively. Sky conditions were near-photometric for each observation, and the data were acquired near the center of the track to maximize the primary mirror illumination. After subtracting a sky frame, the images were collapsed in the spatial dimension to sum the pixel counts and a wavelength solution was applied. For each wavelength bin, the detected number of photons was compared to the expected number of photons from the standard star to provide the total sky-to-detector system throughput, which is plotted along with the modeled throughput in Fig. 18*a*. The overall shape of

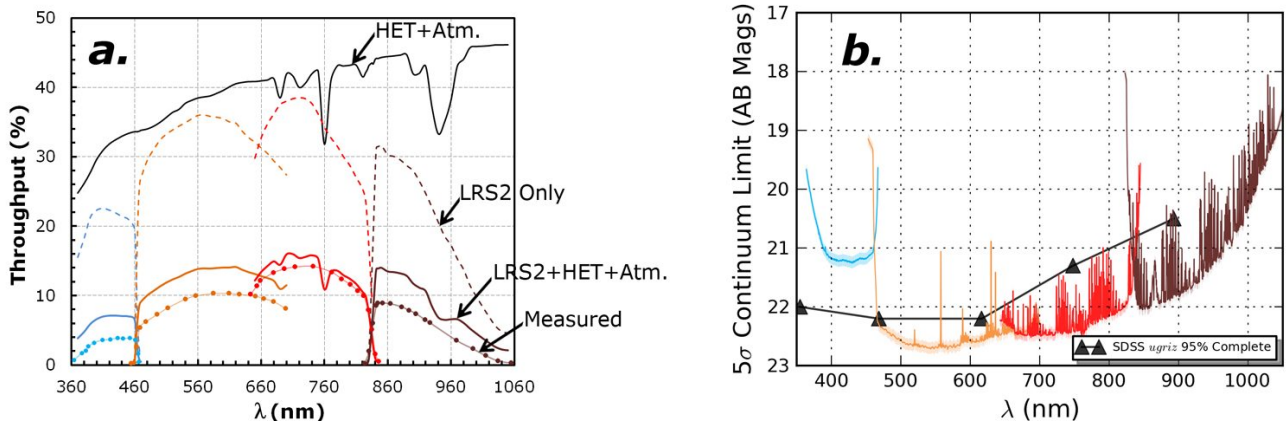

Figure 18. *a*) Modeled throughput for LRS2. The solid black curve shows the transmission of the atmosphere combined with the HET. The dashed colored curves show the expected throughput of LRS2 only, from the IFU input to the CCD detector. The solid colored curves are the expected sky-to-detector system throughput. The dotted curves show on-sky measurements of the sky-to-detector system throughput, where the data points show the measurements in between stellar and atmospheric absorption lines. *b*) Using the measured throughput in Panel *a*, the predicted 5σ continuum sensitivity of LRS2 is calculated for a 2×30 minute expsure in $1.65''$ seeing with a 75% telescope pupil illumination factor. The black triangles show the 95% completeness limit for point sources in the SDSS DR10 *ugriz* imaging survey.

the measured throughput for each channel matches the model expectation quite well. However, each channel is slightly under-performing the expected efficiency. The poorer performance of the UV Arm is consistent with the poorer measured coupling efficiency of the IFU (as measured in Sec. 4.4), and both the UV and Orange Arms contain VIRUS CCDs that are somewhat degraded (as described in Sec. 4.6.4). One possible reason for an overall degradation of the system throughput compared to the expectation is the current state of the HET primary mirror compared to the assumptions in the throughput model. The mirror segments are in need of new coatings and have been subjected to unusual conditions within the telescope dome due to the ongoing work associated with the WFU. However, even with no further improvement in the system throughput, LRS2 is currently performing at a comparable or higher level than the best performance delivered by the original LRS instrument. In addition, for all channels except the UV Arm, insertion of the measured throughput curves into a model of the LRS2 instrumental sensitivity shows that the science requirement of being able to spectroscopically probe the imaging limit of the SDSS can still be met within a total exposure time that can be achieved in a single track. This is illustrated in Fig. 18*b* for a 2×30 minute exposure in typical $1.65''$ seeing conditions with a 75% average telescope pupil illumination factor.

As an example of LRS2 data, Fig. 19 shows the LRS2-R Red Arm portion of the spectrum of the spectrophotometric standard star HD19445 that was used to measure the system throughput described above. The figure shows a raw science data frame (where the two sections of the image that are read-out on separate amplifiers have been stitched together), a zoom-in to show the high quality of the fiber separation, and a single-fiber 1-D extracted spectrum showing atmospheric O_2 A-band absorption on top of the stellar signal. The latter illustrates the high-quality measurements that can be obtained with LRS2 in terms of signal-to-noise ratio and spectral resolution.

6. STATUS & OUTLOOK

In May of 2016, the HET Board of Directors approved entering early science operations with LRS2. As a result, shared-risk observing opportunities were opened to the HET community starting on July 1, 2016. LRS2 is therefore the first facility instrument to be installed and opened for community-wide science operations on the newly upgraded HET. As a result of the enhanced capabilities and acceptable performance of the two LRS2 spectrograph pairs, LRS2 will be a worthy replacement for the workhorse LRS instrument. With the new spectroscopic and imaging capabilities coming on line through the HET WFU,[5] LRS2 will add broadband

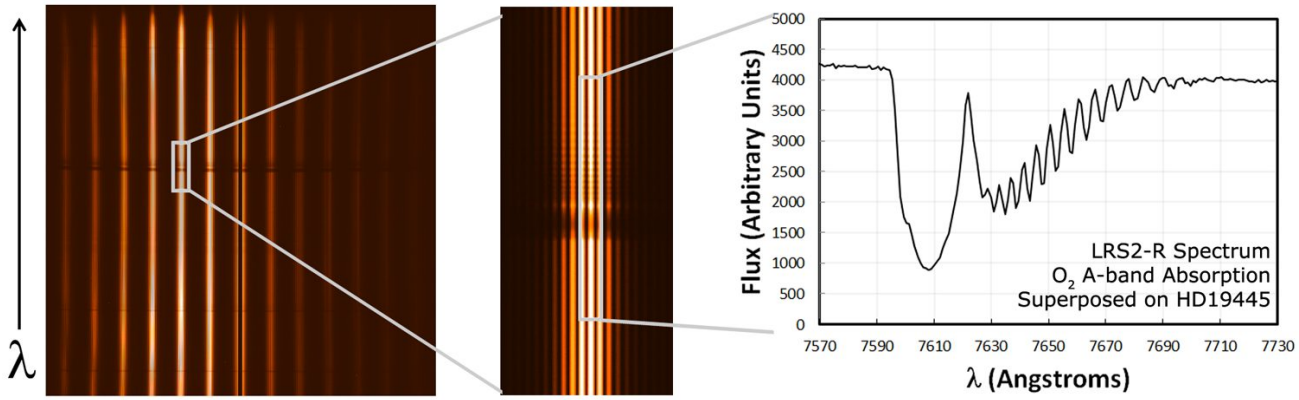

Figure 19. An example of LRS2 data, as illustrated using the LRS2-R Red Arm. At left is a raw science data frame, showing the spectra of the spectrophotometric standard star HD19445. The dispersion is in the vertical direction, and many fibers are illuminated for the individual point source target due to the fine spatial sampling of the IFU. The middle panel shows a zoom-in near the brightest bank of fibers around the absorption associated with the atmospheric O_2 A-band. The panel at right shows a section of the 1-D extracted spectrum, which illustrates the high quality of the LRS2 data in terms of signal-to-noise and spectral resolution.

integral field spectroscopic capability in a robust package that will be ideal for survey follow-up in the HETDEX era.

ACKNOWLEDGMENTS

HETDEX is run by the University of Texas at Austin McDonald Observatory and Department of Astronomy with participation from the Ludwig-Maximilians-Universität München (LMU), Max-Planck-Institut für Extraterrestriche-Physik (MPE), Leibniz-Institut für Astrophysik Potsdam (AIP), Texas A&M University (TAMU), Pennsylvania State University (PSU), Institut für Astrophysik Göttingen (IAG), University of Oxford, Max-Planck-Institut für Astrophysik (MPA), and The University of Tokyo. In addition to Institutional support, HETDEX is funded by the National Science Foundation (grant AST-0926815), the State of Texas, the US Air Force (AFRL FA9451-04-2-0355), the Texas Norman Hackerman Advanced Research Program under grants 003658-0005-2006 and 003658-0295-2007, and generous support from private individuals and foundations.

We thank the staffs of McDonald Observatory, HET, AIP, MPE, TAMU, IAG, Oxford University Department of Physics, the University of Texas Center for Electromechanics, and the University of Arizona College of Optical Sciences for their contributions to the development of the HET WFU and VIRUS.

Financial support for innoFSPEC Potsdam of the German BMBF program *Unternehmen Region* (grant no. 03Z2AN11), and of Land Brandenburg, MWFK, is gratefully acknowledged. We also acknowledge support by the German BMI program *Wirtschaft trifft Wissenschaft*, grant no. 03WWBB105.

This paper is based on the doctoral thesis of T.S.C., which was primarily supported by a National Science Foundation Graduate Research Fellowship.

REFERENCES

[1] Ramsey, L. W. et al., "Early performance and present status of the Hobby-Eberly Telescope," in [*Advanced Technology Optical/IR Telescopes VI*], *Proc. SPIE* **3352-34** (1998).

[2] Hill, G. J. et al., "The Hobby-Eberly Telescope Dark Energy Experiment (HETDEX): Description and Early Pilot Survey Results," in [*Panoramic Views of Galaxy Formation and Evolution*], *ASP Conference Ser.* **399, 115** (2008).

[3] Hill, G. J. et al., "VIRUS: first deployment of the massively replicated fiber integral field spectrograph for the Hobby-Eberly Telescope," in [*Ground-based and Airborne Instrumentation for Astronomy VI*], *Proc. SPIE* **9908-54** (2016).

[4] Lee, H. et al., "Delivery, installation, and on-sky verification of Hobby-Eberly Telescope wide-field corrector," in [*Ground-based and Airborne Telescopes VI*], *Proc. SPIE* **9906-156** (2016).
[5] Hill, G. J. et al., "The Hobby-Eberly Telescope wide-field upgrade," in [*Ground-based and Airborne Telescopes VI*], *Proc. SPIE* **9906-5** (2016).
[6] Good, J. M. et al., "HET wide-field upgrade tracker system performance," in [*Ground-based and Airborne Telescopes VI*], *Proc. SPIE* **9906-167** (2016).
[7] Vattiat, B. L. et al., "Design, alignment, and deployment of the Hobby-Eberly Telescope prime focus instrument package," in [*Ground-based and Airborne Instrumentation for Astronomy V*], *Proc. SPIE* **9147-172** (2014).
[8] Hill, G. J. et al., "The Hobby-Eberly Telescope low-resolution spectrograph," in [*Optical Astronomical Instrumentation*], *Proc. SPIE* **3355-375** (1998).
[9] Shetrone, M. D. et al., "Ten Year Review of the Queue Scheduling of the Hobby-Eberly Teelescope," *PASP* **119, 556** (2007).
[10] Hill, G. J. et al., "Performance of the Hobby-Eberly Telescope and facility instruments," in [*Ground-based Instrumentation for Astronomy*], *Proc. SPIE* **5492, 94** (2004).
[11] Schaefer, B. E. et al., "GRB 021004: a Massive Progenitor Star Surrounded by Shells," *ApJ* **588, 387** (2003).
[12] Racusin, J. L. et al., "Broadband observations of the naked eye γ-ray burst GRB080319B," *Nature* **455, 183** (2008).
[13] Kaspi, S. et al., "Reverberation Mapping of High-Luminosity Quasars: First Results," *ApJ* **659, 997** (2007).
[14] Quimby, R. M. et al., "SN 2005ap: A Most Brilliant Explosion," *ApJ* **668, L99** (2007).
[15] Luhman, K. L. et al., "An Infrared/X-Ray Survey for New Members of the Taurus Star-Forming Region," *ApJ* **703, 399** (2009).
[16] Schneider, D. P. et al., "Discovery of a Pair of $z = 4.25$ Quasars from the Sloan Digital Sky Survey," *AJ* **120, 2183** (2000).
[17] Corsini, E. M. et al., "Spatially Resolved Spectroscopy of Coma Cluster Early-type Galaxies. IV. Completing the Data Set," *ApJS* **175, 462** (2008).
[18] Chonis, T. S. et al., "LRS2: the new facility low resolution integral field spectrograph for the Hobby-Eberly Telescope," in [*Ground-based and Airborne Instrumentation for Astronomy V*], *Proc. SPIE* **9147-9** (2014).
[19] Lee, H. et al., "LRS2: a new low-resolution spectrograph for the Hobby-Eberly Telescope," in [*Ground-based and Airborne Instrumentation for Astronomy III*], *Proc. SPIE* **7735-276** (2010).
[20] Chonis, T. S. et al., "Design and construction progress of LRS2-B: a new low resolution integral field spectrograph for the Hobby-Eberly Telescope," in [*Ground-based and Airborne Instrumentation for Astronomy IV*], *Proc. SPIE* **8446-103** (2012).
[21] Chonis, T. S. et al., "Mass production of volume phase holographic gratings for the VIRUS spectrograph array," in [*Advances in Optical and Mechanical Technologies for Telescopes and Instrumentation*], *Proc. SPIE* **9151-53** (2014).
[22] Hill, G. J. et al., "Design, construction, and performance of VIRUS-P: the prototype of a highly replicated integral field spectrograph for the HET," in [*Ground-based and Airborne Instrumentation for Astronomy II*], *Proc. SPIE* **7014-257** (2008).
[23] Adams, J. J. et al., "The HETDEX Pilot Survey. I. Survey Design, Performance, and Catalog of Emission-Line Galaxies," *ApJS* **192, 5** (2011).
[24] Hill, G. J. et al., "Volume Phase Hoographic Grisms for Optical and Infrared Spectrographs," in [*Specialized Optical Developments in Astronomy*], *Proc. SPIE* **4842, 1** (2003).
[25] Mahadevan, S. et al., "The habitable-zone planet finder: status update on the development of a stabalized fiber-fed near-infrared spectrograph for the Hobby-Eberly Telescope," in [*Ground-based and Airborne Instrumentation for Astronomy V*], *Proc. SPIE* **9147-51** (2014).
[26] Kelz, A. et al., "Commissioning of VIRUS integral-field units at the Hobby-Eberly Telescope," in [*Ground-based and Airborne Instrumentation for Astronomy VI*], *Proc. SPIE* **9908-319** (2016).
[27] Murphy, J. D. et al., "The influence of motion and stress on optical fibers," in [*Ground-based and Airborne Instrumentation for Astronomy IV*], *Proc. SPIE* **8446-207** (2012).

[28] Murphy, J. D. et al., "Focal ratio degradation and transmission in VIRUS-P optical fibers," in [*Advanced Optical and Mechanical Technologies in Telescopes and Instrumentation*], *Proc. SPIE* **7018, 2** (2008).
[29] Allington-Smith, J. et al., "Integral Field Spectroscopy with the Gemini Multiobject Spectrograph. I. Design, Construction, and Testing," *PASP* **114, 892** (2002).
[30] Baldry, I. K. et al., "Volume Phase Holographic Gratings: Polarization Properties and Diffraction Efficiency," *PASP* **116, 403** (2004).
[31] Burgh, E. B. et al., "Recombination Ghosts in Littrow Configuration: Implications for Spectrographs Using Volume Phase Holographic Gratings," *PASP* **119, 1069** (2007).
[32] Gaylord, T. K. and Moharam, M. G., "Analysis and applications of optical diffraction by gratings," *Proc. IEEE* **73, 894** (1985).
[33] Prochaska, T. et al., "VIRUS spectrograph assembly and alignment procedures," in [*Ground-based and Airborne Instrumentation for Astronomy IV*], *Proc. SPIE* **8446-193** (2012).
[34] Ramsey, J. et al., "A control system framework for the Hobby-Eberly Telescope," in [*Software and Cyberinfrastructure for Astronomy IV*], *Proc. SPIE* **9913-160** (2016).
[35] Odewahn, S. C. et al., "VIRUS Parallel Observations with the Hobby-Eberly Telescope," in [*American Astronomical Society Meeting Abstracts*], *AAS* **219, 424.18** (2012).
[36] Lee, H. et al., "Final implementation and photon-efficiency verification of Hobby-Eberly Telescope facility calibration unit," in [*Ground-based and Airborne Instrumentation for Astronomy VI*], *Proc. SPIE* **9908-89** (2016).
[37] Lee, H. et al., "Metrology systems of Hobby-Eberly Telescope wide field upgrade," in [*Ground-based and Airborne Telescopes IV*], *Proc. SPIE* **8444-181** (2012).
[38] Snigula, J. M. et al., "Cure-WISE: HETDEX data reduction with Astro-WISE," in [*Software and Cyberinfrastructure for Astronomy II*], *Proc. SPIE* **8451-78** (2012).
[39] Adams, J. J. et al., "Volume phase holographic grating performance on the VIRUS-P instrument," in [*Ground-based and Airborne Instrumentation for Astronomy II*], *Proc. SPIE* **7014, 232** (2008).
[40] Chonis, T. S. et al., "Methods for evaluating the performance of volume phase holographic gratings for the VIRUS spectrograph array," in [*Ground-based and Airborne Instrumentation for Astronomy IV*], *Proc. SPIE* **8446-209** (2012).
[41] Marshall, J. L. et al., "VIRUS instrument collimator assembly," in [*Ground-based and Airborne Instrumentation for Astronomy V*], *Proc. SPIE* **9147-143** (2014).
[42] Tuttle, S. E. et al., "Initial results from virus production spectrographs," in [*Ground-based and Airborne Instrumentation for Astronomy IV*], *Proc. SPIE* **8446-221** (2012).
[43] Tuttle, S. E. et al., "The construction, alignment, and installation of the VIRUS spectrograph," in [*Ground-based and Airborne Instrumentation for Astronomy V*], *Proc. SPIE* **9147-26** (2014).
[44] Kaiser, P., "Spectral Losses of Unclad Fibers Made from High-Grade Vitreous Silica," *Apply. Phys. Lett.* **23**, 45 (1973).
[45] Lee, H. et al., "Visible Integral-field Replicable Unit Spectrograph (VIRUS) optical tolerance," in [*Ground-based and Airborne Instrumentation for Astronomy III*], *Proc. SPIE* **7735-140** (2010).
[46] Lee, H. et al., "Fine optical alignment correction of astronomical spectrographs via in-situ full-field moment-based wavefront sensing," in [*Modern Technologies in Space- and Ground-based Telescopes and Instrumentation II*], *Proc. SPIE* **8450-192** (2012).
[47] Indahl, B. et al., "VIRUS characterization development and results from first batches of delivered units," in [*Ground-based and Airborne Instrumentation for Astronomy VI*], *Proc. SPIE* **9908-299** (2016).
[48] Janesick, J. R., [*Photon Transfer*], Bellingham, Washington: SPIE (2007).
[49] Prochaska, T. et al., "VIRUS instrument enclosures," in [*Ground-based and Airborne Instrumentation for Astronomy V*], *Proc. SPIE* **9147-257** (2014).
[50] Smith, M. P. et al., "The cryogenic system for the VIRUS array of spectrographs on the Hobby-Eberly Telescope," in [*Advanced Optical and Mechanical Technologies in Telescopes and Instrumentation*], *Proc. SPIE* **7018-177** (2008).
[51] Chonis, T. S. et al., "Development of a cryogenic system for the VIRUS array of 150 spectrographs for the Hobby-Eberly Telescope," in [*Ground-based and Airborne Instrumentation for Astronomy III*], *Proc. SPIE* **7735-265** (2010).